MAGEMin, an efficient Gibbs energy minimizer: application to igneous systems

N. Riel[1,2], B.J.P. Kaus[1,2,3], E.C.R. Green[4], and N. Berlie[1]

[1]*Institute of Geosciences, Johannes Gutenberg-University, Mainz, Germany*
[2]*Terrestrial Magmatic Systems (TeMaS) research center, Johannes Gutenberg-University, Mainz, Germany*
[3]*Mainz Institute of Multiscale Modelling (M3ODEL), Johannes Gutenberg-University, Mainz, Germany*
[4]*School of Geography, Earth and Atmospheric Sciences, The University of Melbourne, Victoria 3010, Australia*

This manuscript has been submitted to Geochemistry, Geophysics, Geosystems. This paper is a non-peer reviewed preprint submitted to EarthArXiv. Subsequent version of this manuscript may have different content.

MAGEMin, an efficient Gibbs energy minimizer: application to igneous systems

N. Riel[1,2], B.J.P. Kaus[1,2,3], E.C.R. Green[4], and N. Berlie[1]

[1]Institute of Geosciences, Johannes Gutenberg-University, Mainz, Germany
[2]Terrestrial Magmatic Systems (TeMaS) research center, Johannes Gutenberg-University, Mainz, Germany
[3]Mainz Institute of Multiscale Modelling (M3ODEL), Johannes Gutenberg-University, Mainz, Germany
[4]School of Geography, Earth and Atmospheric Sciences, The University of Melbourne, Victoria 3010, Australia

Key Points:

- A new, parallel, Gibbs energy minimization approach is presented to compute multiphase multicomponent equilibria
- It predicts parameters like stable phases, melt content or seismic velocities as a function of chemistry and temperature/pressure conditions
- Examples and benchmark cases are presented that apply the approach to magmatic systems

Plain Language Summary

Understanding magmatic systems requires knowing how rocks melt. Because a single melting experiment can easily take weeks, it is impossible to do enough experiments to cover the whole range of pressure, temperature and composition relevant for magmatic systems. We therefore need a way to interpolate in between conditions that are not directly covered by the experiments. It is long known that the best way to perform such interpolation is by using basic thermodynamic principles. For magmatic systems, this requires a well-calibrated thermodynamic melting model. It also requires an efficient computational tool to predict the most stable configuration of minerals and melt. Since the 1980's a number of such computational tools have been developed to perform a so-called Gibbs energy minimization. These tools work very well for simpler systems but become very slow for recently developed, more realistic, melting models. Here, we describe a new method that combines some ideas of the previous methods with a new algorithm. Our method is faster and takes advantage of modern computer architectures. It can predict rock properties such as densities, seismic velocities, melt content and chemistry. It can therefore be used to link physical observations with hard-rock data of magmatic systems.

Corresponding author: N. Riel, nriel@uni-mainz.de

Abstract

Prediction of stable mineral equilibria in the Earth's lithosphere is critical to unravel the tectonomagmatic history of exposed geological sections. While the recent advances in geodynamic modelling allow us to explore the dynamics of magmatic transfer in solid mediums, there is to date no available thermodynamic package that can easily be linked and efficiently accounts for the computation of phase equilibrium in magmatic systems. Moreover, none of the existing tools fully exploit single point calculation parallelization which strongly hinders their applicability for direct geodynamic coupling or for thermodynamic database inversions. Here, we present a new Mineral Assemblage Gibbs Energy Minimizer (MAGEMin). The package is written as a parallel C library, provides a direct Julia interface and is callable from any petrological/geodynamic tool. For a given set of pressure, temperature and bulk-rock composition MAGEMin uses a combination of linear programming, extended Partitioning Gibbs Energy and gradient-based local minimization to compute the stable mineral assemblage. We apply our new minimization package to the igneous thermodynamic dataset of (Holland et al., 2018) and produce several phase diagrams at supra-solidus conditions. The phase diagrams are then directly benchmarked against THERMOCALC and exhibit very good agreement. The high scalability of MAGEMin on parallel computing facilities opens new horizons e.g., for modelling reactive magma flow, for thermodynamic dataset inversion and for petrological/geophysical applications.

1 Introduction

The thermodynamic modelling of equilibrium mineral assemblages is a crucial tool for understanding the solid Earth. Mineral equilibrium modelling can be used in an inverse sense, to make inferences about magmatic and tectonic processes based on the rocks that they generated. Used in a forward-modelling sense, our capacity to simulate Earth processes is greater if we can model the most stable mineral assemblage under given conditions, since the mineral assemblage controls or contributes to the thermodynamic, chemical and rheological properties of the rock package. Such modelling thus forms a key step in linking geophysical observations with petrological constraints, and to assess the effect of mineral reactions on deformation of the lithosphere. Even when geological systems are not always at equilibrium, non-equilibrium effects tends to move the system towards equilibrium (Lasaga, 1986), and as such it remains crucial to be able to efficiently model the equilibrium state (e.g., Hou et al., 2021).

In order to model mineral equilibria, an equation of state is needed for each mineral or fluid phase that might potentially be stable under the conditions of interest. The equation of state describes the calorimetric and volumetric properties of the phase as a function of its pressure, temperature, composition and state of order. A phase may be considered to have anything from one compositional components (a pure phase) up to the maximum number of components in which the rock system is to be modelled. It may or may not contain dimensions of order-disorder. There are several different thermodynamic datasets currently in use that comprise collections of such equations of state, usually aimed at modelling a subset of terrestrial mineral equilibria; for example those of R. W. White et al. (2014) (equilibria in metapelites), Green et al. (2016) (equilibria in metabasites), and Stixrude and Lithgow-Bertelloni (2011), Stixrude and Lithgow-Bertelloni (2021) (equilibria among mantle phases). Each collection is calibrated with some degree of internal consistency. In this contribution we use a version of the thermodynamic dataset of Holland et al. (2018), which incorporates the internally-consistent dataset of end-member thermodynamic properties of Holland and Powell (2011) and Tomlinson and Holland (2021). However, our method can also be applied to any other thermodynamic datasets.

Mineral equilibrium calculations for geological applications commonly assume that pressure and temperature are the independent variables in the problem, rather than their

conjugates, volume and entropy. Therefore, the equilibrium compositions and states of order for the phases in a model equilibrium are found by minimizing the Gibbs energy, G, of the assemblage. However, minimization of the Gibbs energy in multicomponent and multiphase systems remains one of the most challenging global optimization problems, not only in the fields of metamorphic petrology (e.g., Lanari & Duesterhoeft, 2018), but also for chemical engineering (e.g., Fateen, 2016; Lothenbach et al., 2019) and for the nuclear industry (e.g., Piro, 2011; Piro et al., 2013). Because the problem is intrinsically multidimensional, non-linear and non-convex, minimization strategies are not guarantee to obtain the global minimum of the Gibbs energy of the system. Consequently, numerous Gibbs energy minimization strategies are used depending on the problem dimensionality (number of chemical components) and complexity of the equations of state. This includes, but is not limited to, equality and non-equality contrained linear least squares (e.g., Ghiorso, 1983, 1985), linear programming and non-linear optimization methods (e.g., de Capitani & Brown, 1987), discretization of the equations of state in composition–order space combined with linear programming (e.g., Connolly, 1990; Connolly, 2005), linear programming and Partitioning Gibbs Energy (e.g., Piro, 2011; Piro et al., 2013; Kruskopf & Visuri, 2017), metaheuristic optimization methods (e.g., Teh & Rangaiah, 2002; Burgos-Solórzano et al., 2004; Çetin & Keçebaş, 2021) and Lagrangian formulations (e.g., W. White et al., 1958; Piro & Simunovic, 2016).

In the geosciences, a number of petrological tools have been developed to predict phase equilibria, study phase relations and produce phase diagrams, e.g., Gibbs (Spear, 1988), thermocalc (Powell & Holland, 1988), Perple_X (Connolly, 1990; Connolly, 2005), Theriak-Domino (de Capitani & Brown, 1987; de Capitani & Petrakakis, 2010), MELTS and pMELTS (Ghiorso, 1983, 1985; Ghiorso & Sack, 1995; Asimow & Ghiorso, 1998), GeoPS (Xiang & Connolly, 2021). In general, they fall into two categories (Connolly, 2017; Lanari & Duesterhoeft, 2018): phase equilibrium calculators and Gibbs energy minimizers.

The first category (e.g., thermocalc and Gibbs) equate the chemical potentials of components in a specified set of phases, in order to calculate what compositions and states of order the phases must have, to be in equilibrium with each other under the specified conditions. The user may investigate any set of phases for which equations of state are present within the thermodynamic dataset. Conditions to be specified might include pressure, temperature, bulk system composition, or partial phase compositions. Univariant reactions or other phase field boundaries are calculated using geometric constraints (Schreinemakers analysis or related rules) combined with experience and a priori knowledge of the petrological system. This approach allows a wide range of phase diagrams to be calculated, and facilitates the user in exploring any equilibrium of interest, whether stable or metastable. However, in many applications in the geosciences, the only equilibrium of interest is that of the most stable equilibrium at given bulk system composition – or, in geological terms, the most stable equilibrated mineral assemblage in a given bulk rock composition. The phase equilibrium calculator approach is not optimal for this purpose, since it depends on the user anticipating all of the phases that might appear in the stable equilibrium. In complex systems, even an expert user may easily overlook the presence of a phase in a given region of the diagram, and consequently mistake a metastable assemblage for the stable one. Programs in the second category (e.g., MELTS, pMELTS, Theriak-Domino, Perple_X and GeoPS) are designed specifically to predict the most stable assemblage in a given bulk rock composition. At each point on a pressure–temperature grid, these programs explore all possible equilibria among subsets of the phases in a large pre-specified list, potentially including all the phases represented in the thermodynamic dataset. They return the subset of these phases that yield the lowest Gibbs energy for the system, along with equilibrium phase compositions and states of order.

Three main Gibbs energy minimization approaches are commonly used in the geosciences. MELTS and pMELTS (Ghiorso, 1983, 1985; Ghiorso & Sack, 1995; Asimow &

Ghiorso, 1998) use Taylor series expansion to express the Gibbs energy of the system and minimize the resulting system of constrained linear equations using least squares methods. However, the thermodynamic datasets hard-wired into MELTS and pMELTS are relatively limited in their application, as they are not appropriate for handling subsolidus equilibria, nor equilibria involving amphibole or biotite. Theriak-Domino uses a combination of linear programming and non-linear local optimization methods (de Capitani & Brown, 1987) to compute the phase equilibria. Perple_X (Connolly, 2005) linearizes the problem by discretizing the equations of state in composition–order space, and solves it using the simplex algorithm. A detailed review of Perple_X and Theriak-Domino methods is presented in Connolly (2017). While these two approaches have proven to be quite reliable and efficient in systems involving a limited number of components, their performance and reliability tends to decrease for higher dimensional systems. For Theriak-Domino the main limitation can be attributed to the absence of constraints during the rotation of the Gibbs-hyperplane between the linear programming and non-linear optimization stages. For Perple_X, discretization becomes increasingly expensive as the number of compositional components in the equations of state becomes larger. GeoPS (Xiang & Connolly, 2021) has recently been successful in combining these two approaches to provide the community with an efficient petrological program to easily compute phase diagrams. However, none of the above tools are MPI-parallelized for single point calculations, they are not designed to fully exploit high performance facilities, which constitutes a critical limitation for direct coupling with geodynamic modelling. The recent breakthroughs in modelling coupled mechanical and fluid/magma flow systems (e.g., Keller et al., 2013; Taylor-West & Katz, 2015; Keller & Katz, 2016; Keller et al., 2017; Turner et al., 2017; Keller & Suckale, 2019; Rummel et al., 2020; Katz et al., 2022), and, the ongoing open-source movement in the community to simplify and unify modelling tools (e.g., Bezanson et al., 2017, Julia) however, highlight the need for an efficient, open-source and fully parallel mineral assemblage modelling routine.

Here, we describe a new approach, MAGEMin (Mineral Assemblage Gibbs Energy Minimization) (https://github.com/ComputationalThermodynamics/MAGEMin.git), which was developed to provide a minimization routine that is easily callable and fulfils several objectives. First, the package performs single point calculations at given pressure, temperature and bulk-rock composition and finds the thermodynamically most stable assemblage in an automated manner with no required a priori knowledge of the system which is a requirement for integration with geodynamic software. Second, the package has been developed for stability, performance and scalability in complex chemical systems.

Our Gibbs minimization approach combines discretization of the equations of state in composition space (Connolly, 1990) with linear programming (de Capitani & Brown, 1987), and extends the mass constrained Gibbs-hyperplane rotation (Piro et al., 2013) method to account for the mixing on crystallographic sites that takes place in silicate mineral solid solutions. In this way, we overcome many of the drawbacks of the above-mentioned software packages. Moreover, since the method is developed around point-wise calculations, it is well-suited for parallelization on massively parallel machines and can be combined with an adaptive mesh refinement strategy. We demonstrate the effectiveness of our method by computing a series of phase diagrams using a large thermodynamic dataset native to the THERMOCALC software, and comparing the automatically calculated MAGEMin results with those obtained using THERMOCALC. The definition of the general terminology used in this contribution is given in Table 1 and the definition of the symbols is provided in Table 2.

Table 1. General terminology

Term	Definition
System component	Chemically independent constituent (see Pauken (2011)). The collection of components define the number of chemical dimensions of the system. Here, we use oxides as system components spanning up to 11 dimensions: Na_2O–CaO–K_2O–FeO–MgO–Al_2O_3–SiO_2–TiO_2–Fe_2O_3–Cr_2O_3–H_2O.
Pure phase	(or stoichiometric phase), is a phase that has a fixed composition (or does not vary measurably from its ideal composition) e.g., quartz (SiO_2)
End-member	(or species (Kruskopf & Visuri, 2017) or phase component (Berman, 1991), or vertex of a polytope (Myhill & Connolly, 2021)) is an independent instance of a solution phase (with defined cation occupancy/vacancy on each site) that can be linearly combined with other end-members to span the complete site-occupancy space of a solution
Solution phase	A Solution phase is a mixture of end-members spanning a range of compositions for a single crystal structure (solid solution phase), a fluid or a melt. For instance, in a chemical sub-system restricted to FeO–MgO–SiO_2, the compositional space of olivine is covered by the linear mixture of fayalite (Fe_2SiO4) and forsterite (Mg_2SiO4) end-members. The composition of the end-members are expressed in oxide form (fayalite = 2FeO + SiO_2 and forsterite = 2MgO + SiO_2) but the substitution of Fe and Mg cations occurs in elemental form on the olivine crystallographic site M1 ($[Fe,Mg]^{M1}$ SiO_2)
Pseudosection	(or isochemical equilibrium phase diagram (de Capitani & Brown, 1987)) is a class of phase diagram in pressure-temperature space showing the fields of most stable phase equilibrium for a single bulk-rock composition
Solution phase model	(or equation of state (Powell, 1978)) aims to reproduce the energetic behaviour of naturally occurring mineral, melt, and fluid phases. Depending on the complexity of the phase of interest, the related solution phase model is usually formulated using an ideal and a non-ideal mixing term
Ideal mixing term	The ideal mixing term include both the mechanical mixture contribution, which is the linear combination of the standard Gibbs energy of the end-members, and the configurational energy term which describes the change of energy when the mixture reacts to form a single phase (see Ganguly (2001) and Lanari and Duesterhoeft (2018) for more details)
Non-ideal mixing term	(or excess term) expresses the non-ideal interaction between end-members (see Ganguly (2001))

2 Methodology

2.1 Gibbs energy formulation

At fixed pressure P and temperature T, the integral Gibbs energy [J] of a multi-component multiphase system G_{sys} (e.g., Gibbs, 1878; Spear, 1993) can be expressed by:

$$G_{\text{sys}} = \sum_{\lambda=1}^{\Lambda} \alpha_\lambda \sum_{i=1}^{N_\lambda} \mu_{i(\lambda)} p_{i(\lambda)} + \sum_{\omega=1}^{\Omega} \alpha_\omega \mu_\omega, \tag{1}$$

where Λ indicates the number of solution phases (mineral phases of variable composition), N_λ the number of end-members of solution phase λ, Ω the number of pure phases (mineral phases of fixed composition, also described as pure phases), α_λ and α_ω are the mole fractions of solution phase λ and pure phase ω, respectively. $p_{i(\lambda)}$ is the fraction of end-member i dissolved in solution phase λ and $\mu_{i(\lambda)}$, μ_ω are the chemical potential of end-member i in solution phase λ and pure phase ω, respectively. An end-member is defined as an independent instance of a solution phase. In a given chemical system, the linear combination of the end-members span the complete crystallographic site-occupancy space of the solution phase.

The chemical potential of a phase is either a constant for a stoichiometric phase (Spear, 1993):

$$\mu_\omega = g^0_\omega, \tag{2}$$

or a function for a dissolved end-members within a solution phase (see Ganguly, 2001, for a review)

$$\mu_{i(\lambda)} = g^0_{i(\lambda)} + RT\log(a^{id}_{i(\lambda)}) + g^{\text{ex}}_{i(\lambda)}, \tag{3}$$

where R [Jmol^{-1}K^{-1}] is the ideal gas constant, T [K] is the absolute temperature, $a^{id}_{i(\lambda)}$ is the ideal mixing term, $g^0_{i(\lambda)}$ the Gibbs energy of reference of the pure end-member (Helgeson, 1978; Holland & Powell, 1998) and $g^{\text{ex}}_{i(\lambda)}$ is the excess energy term (Powell & Holland, 1993; Holland & Powell, 2003). The ideal mixing term $a^{id}_{i(\lambda)}$ is generally defined as $a^{id}_{i(\lambda)} = p_{i(\lambda)}$ for molecular mixing, or else for mixing on crystallographic sites as

$$a^{id}_{i(\lambda)} = c_i \prod_s (X^s_{e_{s,i}})^{\nu_s} \tag{4}$$

where $X^s_{e_{s,i}}$ is the site fraction of the element $e_{s,i}$ that appears on site s in end-member i of phase λ, ν_s is the number of atoms contained in mixing site s of λ, and c_i is a normalisation constant that ensures that $a^{id}_{i(\lambda)}$ is unity for the pure end-member i. The total Gibbs energy of solution phase λ is given by

$$G_\lambda = \sum_{i=1}^{N_\lambda} \mu_{i(\lambda)} p_{i(\lambda)}. \tag{5}$$

At equilibrium, all pure phases and dissolved end-members in a solution phase have to satisfy the Gibbs-Duhem rule (e.g., Spear, 1988; Spear, 1993)

$$\mu_{i(\lambda),\omega} = \sum_{j=1}^{C} a_{i,\omega j}\Gamma_j, \tag{6}$$

where Γ_j is the chemical potential of the pure component j. The Gibbs-Duhem rule implies that, at equilibrium, the chemical potential of all end-members of a solution phase must lie on the Gibbs-hyperplane defined by Γ_j. At specified pressure and temperature, the system must satisfy the Gibbs phase rule (e.g., Spear, 1988; Spear, 1993)

$$F = C - \Phi \geq 0, \tag{7}$$

where F is the number of degrees of freedom, C is the number of components (or oxides) and Φ is the total number of phases. Finally, the system must satisfy the mass balance constraint, which implies that the ratio of chemical elements supplied by the phases at their equilibrium compositions and proportions should be equal to that in the specified bulk rock composition b_j

$$\sum_{\lambda=1}^{\Lambda} \alpha_\lambda \sum_{i=1}^{N_\lambda} a_{ij} p_{i(\lambda)} + \sum_{\omega=1}^{\Omega} \alpha_\omega a_{\omega j} - b_j = 0, \tag{8}$$

where a_{ij} and $a_{\omega j}$ are composition vectors for the end-member and system components j and $\alpha_{\lambda,\omega} \geq 0$.

Table 2. Symbols definition

Symbol	Unit	Definition
R	J mol^{-1} K^{-1}	Ideal gas constant
T	K	Temperature
C	-	Total number of chemical components (oxides) in the system
F	-	Number of degrees of freedom (Gibbs-Duhem rule)
j	-	Oxide
b_j	-	Bulk rock composition of oxide j
Φ	-	Total number of active phases
Λ	-	Total number of active solution phases
λ	-	Solution phase
N_λ	-	Number of end-members of solution phase λ
$i(\lambda)$	-	End-member i of solution phase λ
$p_{i(\lambda)}$	mol%	Fraction of end-member i in phase λ
$x_{i(\lambda)}$	-	Penalty formulation for PGE stage of end-member i in phase λ
$x_{k(\lambda)}$	-	Compositional variable k of solution phase λ
Ω	-	Total number of active pure phases
ω	-	Pure phase
α_λ	mol%	Fraction of solution phase λ
α_ω	mol%	Fraction of pure phase ω
a_{ij}	mol	Molar composition of oxide j in end-member i
$a_{\lambda j}$	mol	Molar composition of oxide j in solution phase λ
$a_{\omega j}$	mol	Molar composition of oxide j in pure phase ω
f	-	Normalization factor
a_j	-	Number of atom per oxide j
$e_{i(\lambda)}$	-	Molar composition of end-member i in solution phase λ
ν_s	-	Number of atoms contained in mixing site s of λ
c_i	-	Normalisation constant
G_λ	J	Gibbs energy of the solution phase λ
G^{lvl}	J	Gibbs energy of system during the level stage
G_{sys}	J	Total Gibbs energy of the system
Γ_j	J	Chemical potential of pure oxide j, defining Gibbs-hyperplane
Γ^{lvl}	J	Set of oxide chemical potentials obtained during levelling stage
$g^0_{i(\lambda)}$	J	Gibbs energy of reference of end-member i in phase λ
$a^{id}_{i(\lambda)}$	J	Ideal mixing term
$X^s_{e_{s,i}}$	-	Site fraction of the element $e_{s,i}$ on site s in end-member i of phase λ
$g^{\text{ex}}_{i(\lambda)}$	J	Excess energy term of end-member i in phase λ
$\mu_{i(\lambda)}$	J	Chemical potential of end-member i in phase λ
$\Delta\mu_{i(\lambda)}$	J	Gibbs energy distance of end-member i in phase λ from Gibbs-hyperplane
μ_ω	J	Gibbs energy of pure phase ω
ρ	kg m^{-3}	density
K_b	Pa	Adiabatic bulk modulus
K_s	Pa	Elastic shear modulus
v_p	km s^{-1}	Compressional P-wave velocity
v_s	km s^{-1}	Shear S-wave velocity

2.2 Gibbs energy minimization strategy

For any system of fixed bulk composition, pressure and temperature conditions, the general equilibrium conditions are given by minimizing Eq. 1 while satisfying the Gibbs-Duhem rule (Eq. 6) and mass constraint (Eq. 7). This system of equations yields an equality-

constrained optimization problem that remains notoriously difficult to solve as it involves a weighted sum of objective functions unevenly spanning the dimensional space. To compute the thermodynamic equilibrium conditions we employ a two-stage algorithm. First, we obtain an initial guess using discretized solution phases (pseudocompounds) and linear programming methods (levelling, Fig. 1A,B) and after which a local minimization of solution phases is coupled with the Partitioning Gibbs Energy method (Piro et al., 2013) among predicted stable phases (Fig. 1C).

2.2.1 Levelling stage

The concept of levelling is to temporarily neglect the thermodynamic contribution from mixing in the solution phases (de Capitani & Brown, 1987; Piro et al., 2013; Kruskopf & Visuri, 2017). As a consequence, all end-members of solution phases and stoichiometric phases in the system are initially treated as separate pure phases. This allows us to estimate the chemical potential of system components (oxides) and the proportions of the stable pure phases using linear programming methods.

Given this set of artificial "pure phases", the first step of the levelling stage minimizes

$$G^{\text{lvl}} = \min \left(\sum_{\phi=1}^{\Phi} \alpha_\phi g_\phi^0 \right), \tag{9}$$

where Φ is the number of active phases equal to the number of system components C, α_ϕ is the fraction of phase ϕ and g_ϕ^0 is the chemical potential of phase ϕ, and, subject to the mass balance constraint

$$\sum_{\phi=1}^{\Phi} \alpha_\phi a_{\phi j} - b_j = 0, \tag{10}$$

where $a_{\phi j}$ is the composition vector of the phase ϕ and $\alpha_\phi \geq 0$. Equations 9 and 10 are solved using the linear programming method adapted from de Capitani and Brown (1987) with a special case of the simplex method (Dantzig, 1963). Upon convergence, the chemical potential of the system components defining the Gibbs-hyperplane are retrieved such as

$$\Gamma^{\text{lvl}} = A^{-1} G^{\text{lvl}}, \tag{11}$$

where A is the stoichiometry matrix of the predicted stable pure phases and G^{lvl} is the Gibbs energy vector of the same set of pure phases.

During the second step of the levelling stage, solution phases are discretized (pseudocompound) and only the pseudocompounds located close or below the Gibbs-hyperplane defined by Γ^{lvl} are further considered for a second round of linear programming. The distance of a pseudocompound with respect to the Gibbs-hyperplane is calculated as

$$\Delta G_\lambda = \sum_{j=1}^{C} a_{\lambda j} \Gamma_j^{\text{lvl}} - G_\lambda, \tag{12}$$

where $a_{\lambda j}$ is the composition and G_λ is the Gibbs energy of the pseudocompound.

Likewise, the distance from the Gibbs-hyperplane can be calculated for each end-member dissolved in a solution phase from

$$\Delta \mu_{i(\lambda)} = \mu_{i(\lambda)} - \sum_{j=1}^{C} a_{\lambda j} \Gamma_j = g_{i(\lambda)}^0 + RT \log(a_{i(\lambda)}^{id}) + g_{i(\lambda)}^{\text{ex}} - \sum_{j=1}^{C} a_{\lambda j} \Gamma_j. \tag{13}$$

Cycling through the list of pseudocompounds is achieved until no remaining pseudocompound is left with a negative $\Delta G_\lambda \leq -10^{-6}$. The levelling stage is then successfully terminated and the Partitioning Gibbs Energy (PGE) stage is initiated.

2.2.2 Partitioning Gibbs energy (PGE) stage

The Partitioning Gibbs Energy (PGE) approach (e.g., Piro et al., 2013; Kruskopf & Visuri, 2017) has the objective to partition the Gibbs energy of the system among the system components (i.e., Γ_j) by expressing the end-member fraction of the mass balance (Eq. 8) as function of the chemical potential of the end-members (Eq. 3). The key advantage of this approach is that a change in Γ_j (which we attempt to find) is directly coupled to the composition of the system, which helps the optimisation process.

For an non-ideal solution model where the ideal mixing term only depends on the end-member fraction (and not the site-fractions) Piro et al. (2013) first expresses the chemical potential of the end-members as function of the Gibbs-Duhem relation by substituting Eq. 6 in Eq. 3 yielding

$$\sum_{j=1}^{C} a_{i(\lambda),j}\Gamma_j = g^0_{i(\lambda)} + RT\log(x_{i(\lambda)}) + g^{\text{ex}}_{i(\lambda)}. \tag{14}$$

Solving this for $x_{i(\lambda)}$ gives

$$x_{i(\lambda)} = \exp\left(\Big(\sum_{j=1}^{C} a_{\lambda j}\Gamma_j - g^0_\lambda - g^{\text{ex}}_\lambda\Big)/(RT)\right), \tag{15}$$

which is a direct expression of the end-member fraction $x_{i(\lambda)}$ as function of its chemical potential and the chemical potential of the pure components of the system Γ_j. This expression is then substituted into the mass balance equation (Eq. 8) yielding a set of equations (one per component) in the PGE form:

$$\sum_{\lambda=1}^{\Lambda}\alpha_\lambda\sum_{i=1}^{N_\lambda} a_{ij}\exp\left(\Big(\sum_{j=1}^{C} a_{\lambda j}\Gamma_j - g^0_\lambda - g^{\text{ex}}_\lambda\Big)/(RT)\right) + \sum_{\omega=1}^{\Omega}\alpha_\omega a_{\omega j} - b_j = 0, \tag{16}$$

This formulation has proven to be very successful in large chemical systems involving as many as 118 components (Piro, 2011) and relatively simple ideal and non-ideal solution models (Piro et al., 2013; Kruskopf & Visuri, 2017), allowing to model for the first time the temporal and spatial evolution of coupled thermochemical and nuclear reactions of irradiated fuel (Piro et al., 2013).

However, this formulation cannot be directly applied to more complex solid solutions, in which mixing-on-sites must be considered, yielding an ideal entropy term that must be written in terms of site fractions (Eq. 4). To extend the PGE approach to account for solution models involving site-fractions, we expand the ideal mixing term as

$$RT\log(a^{id}_{i(\lambda)}) = RT\log(x_{i(\lambda)}) + RT\log\left(\frac{a^{id}_{i(\lambda)}}{p_{i(\lambda)}}\right), \tag{17}$$

where $x_{i(\lambda)} = p_{i(\lambda)}$, which gives using Eq. 3 and the Gibbs-Duhem relation of Eq. 6

$$RT\log(x_{i(\lambda)}) = \sum_{j=1}^{C} a_{i(\lambda)j}\Gamma_j - g^0_{i(\lambda)} - RT\log\left(\frac{a^{id}_{i(\lambda)}}{p_{i(\lambda)}}\right) - g^{\text{ex}}_{i(\lambda)}. \tag{18}$$

Developing the log term of the right side of Eq. 18 gives

$$RT\log(x_{i(\lambda)}) = \sum_{j=1}^{C} a_{i(\lambda)j}\Gamma_j - g^0_{i(\lambda)} - RT\log(a^{id}_{i(\lambda)}) - g^{\text{ex}}_{i(\lambda)} + RT\log(p_{i(\lambda)}), \tag{19}$$

which can be simplified using Eq. 13 as

$$\log(x_{i(\lambda)}) = -\frac{\Delta\mu_{i(\lambda)}}{RT} + \log(p_{i(\lambda)}), \tag{20}$$

and rearranged as

$$x_{i(\lambda)} = \exp\Big(-\frac{\Delta\mu_{i(\lambda)}}{RT}\Big)p_{i(\lambda)}, \tag{21}$$

where $x_{i(\lambda)}$ is the expression for end-member fraction used in the subsequent PGE formulation and $p_{i(\lambda)}$ is the end-member fraction as computed by the solution phase model. After the levelling stage, and as long as the Gibbs-Duhem constraint is not respected, $\Delta\mu_{i(\lambda)} \neq 0$ and $x_{i(\lambda)} \neq p_{i(\lambda)}$. During the course of the PGE iterations, the term $\exp\Big(-\frac{\Delta\mu_{i(\lambda)}}{RT}\Big)$ tends to 1.0 as $\Delta\mu_{i(\lambda)}$ tends to 0.0, which enforces that at convergence the chemical potential of all the endmembers of predicted stable solution phases lie on the Gibbs-hyperplane (Gibbs-Duhem rule) and that $x_{i(\lambda)} = p_{i(\lambda)}$. The exponential dependency of $x_{i(\lambda)}$ on $\mu_{i(\lambda)}$ imposes the Gibbs-hyperplane computed during levelling to be sufficiently close to solution to ensure convergence.

Eq. (21) is then substituted in Eq. (8) yielding

$$\sum_{\lambda=1}^{\Lambda}\alpha_\lambda\sum_{i=1}^{N_\lambda}a_{ij}x_{i(\lambda)} + \sum_{\omega=1}^{\Omega}\alpha_\omega a_{\omega j} - b_j = 0, \tag{22}$$

which has the advantage that it effectively couples the mass balance constraint (Eq. 8) and the chemical potential of pure components (Eq. 6) (Piro et al., 2013; Kruskopf & Visuri, 2017). Additionally, the sum of the end-member fractions of a solution phase must equal unity at convergence i.e.

$$\sum_{i=1}^{N_\lambda}x_{i(\lambda)} - 1 = 0, \tag{23}$$

and the stoichiometric phases must lie on the Gibbs-hyperplane i.e.

$$\sum_{j=1}^{C}a_{\omega j}\Gamma_j - g^0_\omega = 0. \tag{24}$$

This results in the following system of equations

$$f_v = \sum_{\lambda=1}^{\Lambda}\alpha_\lambda\sum_{i=1}^{N_\lambda}a_{ij}x_{i(\lambda)} + \sum_{\omega=1}^{\Omega}\alpha_\omega a_{\omega j} - b_j, \tag{25}$$

$$h_l = \sum_{i=1}^{N_\lambda}x_{i(\lambda)} - 1, \tag{26}$$

$$q_k = \sum_{j=1}^{C}a_{\omega j}\Gamma_j - g^0_\omega. \tag{27}$$

Eqs. 25, 26 and 27 are solved using a Newton-Raphson approach such as

$$\mathbf{J}\Delta y = -F, \tag{28}$$

where $\mathbf{J}$ is the Jacobian of the system of equations f_v, h_l and q_k expressed as

$$\mathbf{J} = \begin{pmatrix} \frac{\partial f_v}{\partial\Gamma_j} & \frac{\partial f_v}{\partial\alpha_\lambda} & \frac{\partial f_v}{\partial\alpha_\omega} \\ \frac{\partial h_l}{\partial\Gamma_j} & \frac{\partial h_l}{\partial\alpha_\lambda} & \frac{\partial h_l}{\partial\alpha_\omega} \\ \frac{\partial q_k}{\partial\Gamma_j} & \frac{\partial q_k}{\partial\alpha_\lambda} & \frac{\partial q_k}{\partial\alpha_\omega} \end{pmatrix} = \begin{pmatrix} \sum_{\lambda=1}^{\Lambda}\alpha_\lambda\sum_{i=1}^{N_\lambda}x_{i(\lambda)}a_{ij}a_{iv} & \sum_{i=1}^{N_\lambda}x_{i(\lambda)}a_{ij} & a_{\omega j} \\ \sum_{i=1}^{N_\lambda}x_{i(\lambda)}a_{ij} & 0 & 0 \\ a_{\omega j} & 0 & 0 \end{pmatrix}, \tag{29}$$

F is the residual vector defined as

$$F = (f_1, ..., f_C, h_1, ..., h_\Lambda, q_1, ..., q_\Omega), \tag{30}$$

and Δy is the set of variable we solve for

$$\Delta y = (\Delta\Gamma_1, ..., \Delta\Gamma_C, \Delta\alpha_1, ..., \Delta\alpha_\Lambda, \Delta\alpha_1, ..., \Delta\alpha_\Omega). \tag{31}$$

At the beginning of a PGE iteration, all considered solution models are minimized while taking inequality constraints into account. In MAGEMin, we employ the optimization library NLopt (Johnson, 2021) and the gradient-based CCSAQ algorithm (Svanberg, 2002). This algorithm supports inequality constraints which is a requirement to minimize the solution models as the ideal mixing term is function of the site-fractions which have to be ≥ 0. An example of a solution model derivation for a gradient-based inequality constraint optimization is given in the Appendices.

Subsequently, Eq. 28 is solved and the set of variables is updated as $y^1 = y^0 + \tau\Delta y$ where τ is an under-relaxing factor defined as

$$\tau = \min\left(\frac{\frac{0.025}{\delta}}{\left\|\alpha_{\lambda,\omega}^{\max}\right\|_2^2}, \frac{\frac{2.5}{\delta}}{\left\|\Gamma_j^{\max}\right\|_2^2}, 1.0\right), \tag{32}$$

where

$$\delta = 192.0e^{\left[-8.0\cdot\left(\|\Delta b_j\|_2^2\right)^{0.26}\right]} - 1.0, \tag{33}$$

is an inner under-relaxing factor linked to the residual norm of the mass constraint. Effectively, δ decreases the maximum allowed step size of $\Delta\Gamma_j$ and $\Delta\alpha_{\lambda,\omega}$ when the norm of the mass constraint decreases. δ has been optimized in a manual manner across the pseudosections presented in this study to increase the performances and stability of the computation. We choosed this option because the use of backtracking line search methods has proven to be rather inefficient as, in order to converge, the system has to be able to temporarily relax constraints. Although the current definition of δ makes it a proud member of the family of "magic" number, we find that the minimization results remain quite consistent, as long as the relaxing factor is small enough.

During the iterations, a phase is removed from the active assemblage when its fraction is ≤ 0.0 and a phase is added when its driving force ΔG_λ is ≤ 0.0 i.e., the phase has a lower energy than/or is lying on the Gibbs-hyperplane.

The system is considered to have converged when the norm of the mass balance residual vector, the residual of the sum of the end-member fractions and the driving force of the solution phases are lower than 10^{-5}.

2.2.3 Solution phase solvi

Solvi are regions of unmixing within a solution. They can be detected when a stable or metastable assemblage contains two distinct phases with the same structure but different composition, such as co-existing augite and pigeonite for clinopyroxene (e.g. (Gasparik, 2014)). Computationally, the two phases are represented by local minima at two different compositions within a single isobaric-isothermal G-surface of an equation of state. They are handled in several ways.

Firstly, after the levelling stage, if multiple discretized points on the G-surface of the same solution phase are predicted in the stable mineral assemblage they are initially all treated as potential solvi candidates. Subsequently, they are merged after the local minimization step if they converge to the same local minimum ($\|\Delta x_k\|_2^2 \leq 10^{-2}$).

Secondly, during the course of the PGE iterations a solution phase can be duplicated and checked for solvi when its active set of compositional variables is too far from its starting values i.e.,

$$\left\|x_\lambda^t - x_\lambda^0\right\|_2^2 \geq x_{\text{step}}\sqrt{N_x}, \tag{34}$$

where x_λ^t is the actual set of compositional variables, x_λ^0 is the initial set of compositional variables, N_x is the number of compositional variables of solution phase λ and x_{step} is the discretization step of the solution phase λ.

Finally, when getting close to solution $\Delta b_j \leq 10^{-4}$ discretized points of solution phases close to the Gibbs-hyperplane but compositionally away from the active solution phase are locally minimized. In the event the driving force of a tested point $\Delta G_\lambda^{\text{tested}} \leq 0.0$, the point is added to the system. The latter strategy ensures that solvi are not overlooked and that the system converges toward global minimum (no phase lies below the Gibbs-hyperplane).

2.2.4 Failed minimization contingency plan

While local minimization using NLopt (Johnson, 2021) and CCSAQ algorithm (Svanberg, 2002) has proven to be quite efficient and reliable, in some cases the site-fraction inequality constraints can be slightly violated which lead to wrong values of ΔG_λ and $\Delta\mu_{i(\lambda)}$ and therefore to divergence of the overall algorithm.

In order to avoid this, site-fractions are tested after every local minimization of solution phases and in the event a site-fraction is violated, the set of compositional variables is brought back to the feasible domain using the nullspace formulation described in Feppon et al. (2020) such as

$$\Delta x_k = -\alpha_c\Big(\mathbf{G}^T(\mathbf{G}\mathbf{G}^T)^{-1}g\Big), \tag{35}$$

where Δx_k is the compositional variable step toward the feasible domain, g is a vector of violated site-fraction constraints, $\mathbf{G}$ is the Jacobian of the violated site-fractions and $\alpha_c = 0.1$ is an under-relaxing factor. This approach proved to be robust and the solution phase is generally brought back into the feasible domain within 4-5 iterations.

In the event convergence is not achieved using the default tolerance, the tolerance can be relaxed by up to one order of magnitude ($\leq 2 \times 10^{-4}$). If convergence is still not obtained, the minimization is considered to have failed. In all cases a code, MAGEMin sends back the status of the minimization (0, success; 1, relaxed tolerance; 2, failure).

2.3 Dataset implementation

In order to improve performance and benchmark the results with THERMOCALC, the thermodynamic dataset used natively in THERMOCALC was translated directly into C routines for MAGEMin, and implemented without transformation of variables or coordinate systems. This eliminates inconsistencies and minimizes the risk of introducing mistakes. Appendix A gives an overview of equation of state construction in the thermodynamic dataset.

2.4 Normalization for mass balance

Like THERMOCALC, MAGEMin accepts input bulk compositions expressed in terms of normalised numbers of oxide units (SiO_2, Al_2O_3, CaO, ...). However, the phases present in the system at equilibrium will in general be written on a variety of formula units (e.g. (Mg,Fe,Ca)(Mg,Fe)SiO_4, (K,Na,Ca,Mg,Fe)(Mg,Fe,Al,Fe^{3+},Cr)(Si,Al)$_2O_6$, ...). In order to be able to compare the amounts of phases present in a meaningful way, MAGEMin follows THERMOCALC in expressing the amounts of phases present on a 1-atom basis. The Gibbs energies of phases must therefore be normalized.

The normalized Gibbs energy of a model solution phase is expressed as

$$fG_\lambda = f \sum_{i=1}^{N_\lambda} \mu_{i(\lambda)} p_{i(\lambda)}, \tag{36}$$

where f is the normalization factor defined as

$$f = \frac{\sum_{j=1}^{C} b_j a_j}{\sum_{i=1}^{N_\lambda} p_{i(\lambda)} \sum_{j=1}^{C} e_{i(\lambda)j} a_j}, \tag{37}$$

where a_j is the number of atom per oxide and e_i is the molar composition of end-member i of solution phase λ.

The first derivative of the objective function (Eq. 5), necessary to conduct gradient-based minimization, is computed using the chain rule as

$$\frac{\partial f G_\lambda}{\partial x_k} = \left(\mu_{i(\lambda)} - \frac{\sum_{j=1}^{C} e_{i(\lambda)j} a_j}{\sum_{l=1}^{N_\lambda} \sum_{j=1}^{C} e_{l(\lambda)j} a_j} G_\lambda \right) f \frac{\partial p_{i(\lambda)}}{\partial x_k}, \tag{38}$$

where x_k are the compositional variables of solution phase λ.

2.5 Solution phase discretization

The set of pseudocompounds used during the first levelling stage (§2.2.1) and tested when getting close to convergence, is pre-computed using a python Jupyter-Notebook and implemented as C functions to improve performance. The discretization step for each solution phase is chosen to be $0.05 \leq \Delta x_k^{\text{step}} \leq 0.33$ such that the total number of discrete points per solution phase ranges between 100 and 6000 depending of the number of compositional variables (dimensionality). The currently used compositional variables steps for the discretization of the solution phases are: spn, 0.199; bi, 0.124; cd, 0.098; cpx, 0.249; ep, 0.049; g, 0.198; hb, 0.329; ilm, 0.049; liq, 0.198; mu, 0.198; ol, 0.098; opx, 0.249; pl4T, 0.049; as fl is largely dominated by water we only use one pseudocompound made of 100% of the pure water endmember.

3 Algorithm demonstration

To demonstrate how the extended PGE algorithm compares to a linear programming (Theriak-Domino) approach, we present a simplified application in the Na_2O–CaO–K_2O–Al_2O_3–SiO_2 (NCKAS) chemical system. This application includes two pure phases, sillimanite and quartz, and activity–composition (a–x) relations for feldspar (pl4T)(Holland et al., 2021). The bulk-rock composition used in this example is presented in Table 3 as "demo" and the pressure and temperature conditions are fixed at 600 °C and 0.3 GPa.

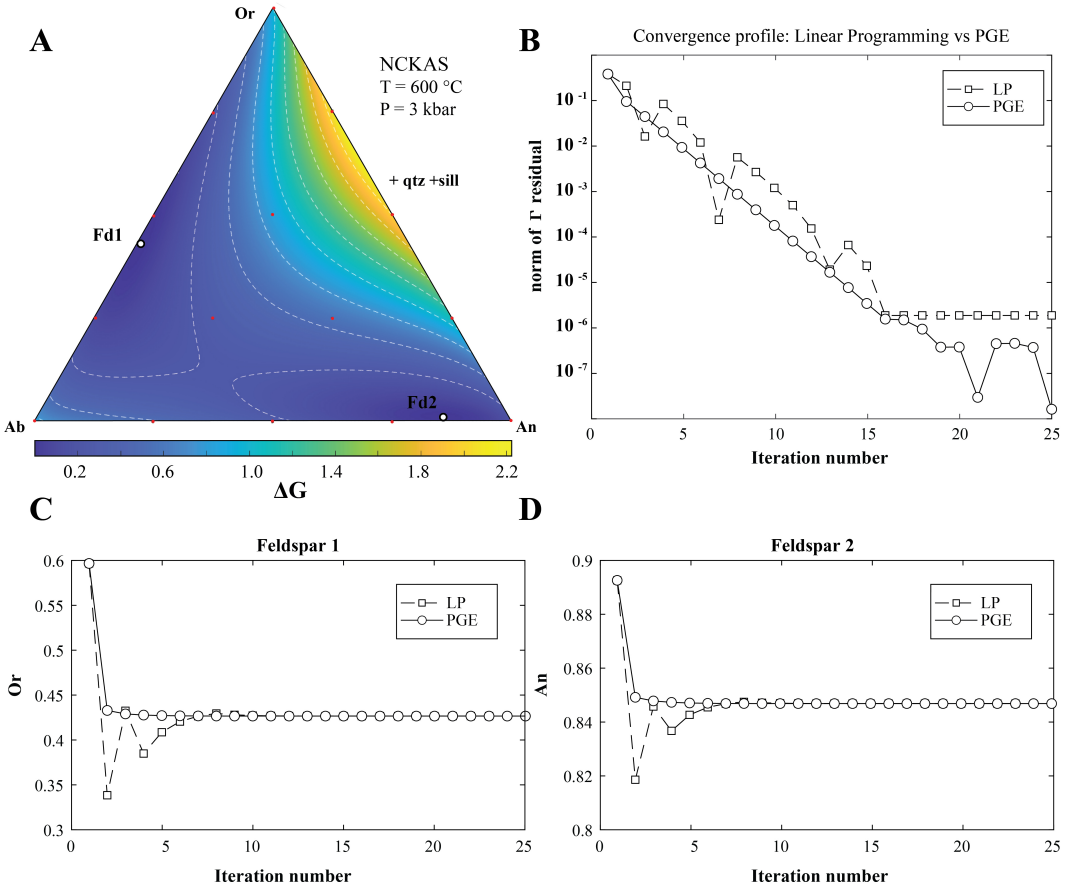

Figure 2. Comparison of Linear Programming (LP) versus the extended Partitioning Gibbs Energy (PGE) approach. A, ΔG energy of the ternary feldspar at equilibrium. "Fd1" and "Fd2" are the two feldspar phases coexisting at equilibrium. The red dots represent the starting set of discretized points of the feldspar solution model for both LP and PGE approach. B, Comparison of the convergence profile between LP and extended PGE approaches. C. Orthose-content of feldspar 1 as function of the minimization iteration. D. Anorthite-content of feldspar 2 as function of the minimization iteration.

The results of the Gibbs energy minimization are shown in figure (2). At equilibrium the Gibbs energy of the system is -1080.8358 J and the mineral assemblage is characterized by quartz (8.123 mol%), sillimanite (9.614 mol%) and two feldspar (41.084 and 41.179 mol%) (Fig. 2). Although both the LP and the PGE methods give very similar results and both exhibit super-linear convergence (Fig. 2B), important differences can be observed. First, the residual on the chemical potential of the system components $\|\Gamma_j\|_2^2$ is, at convergence, one order of magnitude lower with the PGE method (Fig. 2B). Note that the absolute accuracy is controlled by the tolerance of the non-linear optimizer. Here 10^{-10} was used with fmincon MATLAB solver. Secondly, on a log10 basis, the PGE convergence profile is piece-wise linear while the LP profile exhibits significant oscillations (Fig. 2B). The LP oscillations are caused by under/overshooting during local minimization 2C,D) which is not observed for the PGE approach (Figs. 2C,D).

This key difference in convergence behavior between the LP and the PGE methods is related to how the Gibbs-hyperplane is rotated after the gradient-based minimization stage. For the LP method, rotation is achieved by using the Gibbs energy of the min-

imized points irrespective of the chemical potential of their constitutive endmembers (see Eq. 9). Instead, for the extended PGE approach, the rotation is conducted by solving the mass constraint equation where the endmember fractions are penalized using the chemical potentials of the endmembers (see Eq. 8). The additional constraint drive the rotation of the Gibbs-hyperplane in a direction that also decreases the Gibbs-Duhem residual of all species i.e., that the Gibbs-hyperplane of each individual solution phase is rotated to be become parallel to the system Gibbs-hyperplane. This efficiently removes under/overshooting during the non-linear stage (Figs. 2C,D).

This example has been performed with MATLAB using the optimization toolbox and the script is available at https://github.com/ComputationalThermodynamics/sandbox.git

4 Application to igneous systems

Below we demonstrate our approach by presenting a variety of phase diagrams calculations, which we compare with the output from THERMOCALC. Pseudosections map the most stable phase equilibrium to occur in a specified bulk-rock composition, as a function of pressure and temperature. The bulk compositions used in our calculations are shown in Table 3, and are defined in the systems Na_2O–CaO–K_2O–FeO–MgO–Al_2O_3–SiO_2–TiO_2–Fe_2O_3–Cr_2O_3 (NCKFMASTOCr; "dry"), or NCKFMASTOCr+H_2O (NCKFMASHTOCr; "wet").

We used a thermodynamic dataset based on that of Holland et al. (2018), including the minor published updates to the equations of state for solution phases current as of 23 Jan 2022 (see http://hpxeosandthermocalc.org). The updates include a change in the feldspar equation of state to that of Holland et al. (2021). We used version 6.34 of the internally-consistent dataset of end-member thermodynamic properties (Tomlinson & Holland, 2021). The thermodynamic dataset as a whole includes equations of state for the pure stoichiometric phases quartz (q), cristobalite (crst), tridymite (trd), coesite (coe), stishovite (stv), kyanite (ky), sillimanite (sill), andalusite (and), rutile (ru) and sphene (sph). It also represents the solution phases spinel (spn), biotite (bi), cordierite (cd), clinopyroxene (cpx), orthopyroxene (opx), epidote (ep), garnet (g), hornblende (hb), ilmenite (ilm), silicate melt (liq), muscovite (mu), olivine (ol), ternary feldspar (pl4T), and aqueous fluid (fl). An outline of the construction of the thermodynamic dataset is given in Appendix A. Full documentation and THERMOCALC input files for the thermodynamic dataset can be downloaded from http://hpxeosandthermocalc.org, designated as an accompaniment to this paper.

4.1 Example pseudosections

Pseudosections were computed using MAGEMin and processed using an MATLAB Graphical User Interface that employs adaptive mesh refinement similar to what is done in Perple_X (Connolly, 2005)(Fig. 2). The MATLAB application sends a list of pressure-temperature points to MAGEMin for a specified bulk-rock composition and receives back the stable phase mineral assemblage. MAGEMin is parallelized using MPI and can therefore take advantage of multicore processor architectures or be deployed on local or larger remote computing servers.

In total, 6 pseudosections are presented: KLB-1 peridotite (e.g., Takahashi, 1986), RE46 Icelandic basalt (Yang et al., 1996), water-oversaturated tonalite 101 (Piwinskii, 1968), wet basalt and two additional N-MOR basalt (Gale et al., 2013) and MIX1G pyroxenite (Hirschmann et al., 2003). Among them, KLB-1, RE46, wet basalt and Tonalite 101 are directly benchmarked against pseudosections produced with THERMOCALC (Figs. 3 and 4).

Table 3. Bulk-rock compositions (mol%) used to produce the igneous phase diagrams. Note that for readability purpose the Tonalite 101 bulk-rock composition is not displayed normalized to 100.

Name	SiO2	Al2O3	CaO	MgO	FeO	K2O	Na2O	TiO2	O	Cr2O3	H2O
Demo	70.69	16.63	4.56	-	-	4.45	3.67	-	-	-	-
KLB1 peridotite	38.49	1.776	2.824	50.57	5.89	0.01	0.25	0.10	0.096	0.109	-
RE46 basalt	50.72	9.16	15.21	16.25	7.06	0.01	1.47	0.39	0.35	0.01	-
Tonalite 101	66.01	11.98	7.06	4.16	5.30	1.57	4.12	0.66	0.97	0.01	50.0
Water-bearing basalt	50.08	8.69	11.67	12.14	7.78	0.22	2.49	1.00	0.47	0.01	5.44
MIX1G pyroxenite	45.25	8.89	12.22	24.68	6.45	0.03	1.39	0.67	0.11	0.012	-
N-MORB basalt	53.21	9.41	12.2 1	12.21	8.65	0.09	2.90	1.21	0.69	0.02	-

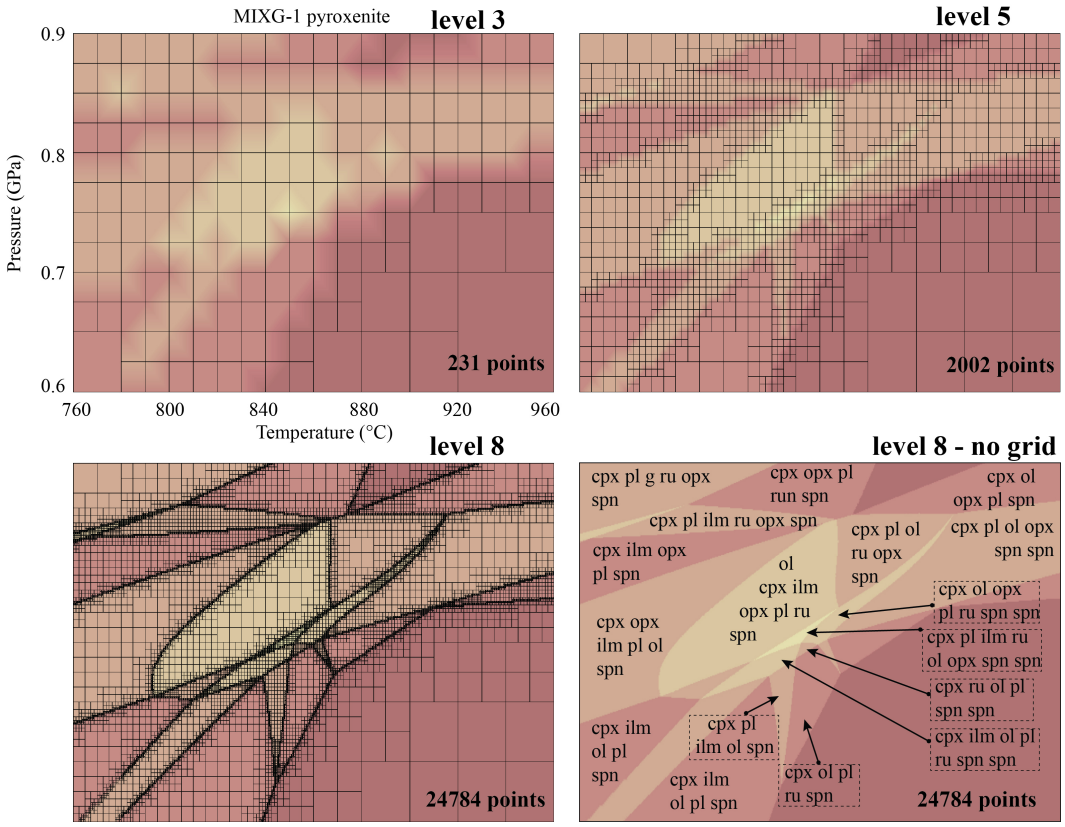

Figure 3. Illustration of the adaptive mesh refinement strategy used for pseudosection computation. Adaptive mesh refinement is illustrated for a sub-section of MIX1G phase diagram displaying complex phase relations (see Fig. 5B). In total 8 levels of refinements are processed with an initial pressure-temperature step of 0.1 GPa and 40 °C. A grid cell is refined by splitting in 4 smaller cells, when at least one of the four corners exhibits a different mineral assemblage. This allows us to progressively increase the resolution along reaction lines and properly resolve them as the levels of refinement increase (see level 8). Moreover, this strategy allows us to significantly reduce the total number of minimization compared to a uniform refinement reaching the same resolution, which would have required 245,760 points for this example.

The pseudosections for KLB-1 peridotite (Fig. 3A,B), RE46 Icelandic basalt (Fig. 3C,D), Tonalite 101 (Fig. 4A,B) and Wet basalt (Fig. 4C,D) were computed with both THERMOCALC and MAGEMin. The pseudosections for KLB-1 and RE46 were computed in the KNCFMASTOCr system from 0 to 5 GPa and from 800 to 2000 °C, and from 0 to 1.2 GPa and from 1000 to 1400 °C, respectively. The pseudosections for T101 and Wet Basalt were computed in the KNCFMASHTOCr system from 0 to 0.25 GPa and from 650 to 925 °C, and from 0 to 2.4 GPa and from 800 to 1400 °C, respectively. For MAGEMin, the total number of minimized points per pseudosection varies from 80,000 to 100,000. The resulting 4 pseudosections produced with MAGEMin show nearly identical results to the one produced with THERMOCALC (Figs 3 and 4).

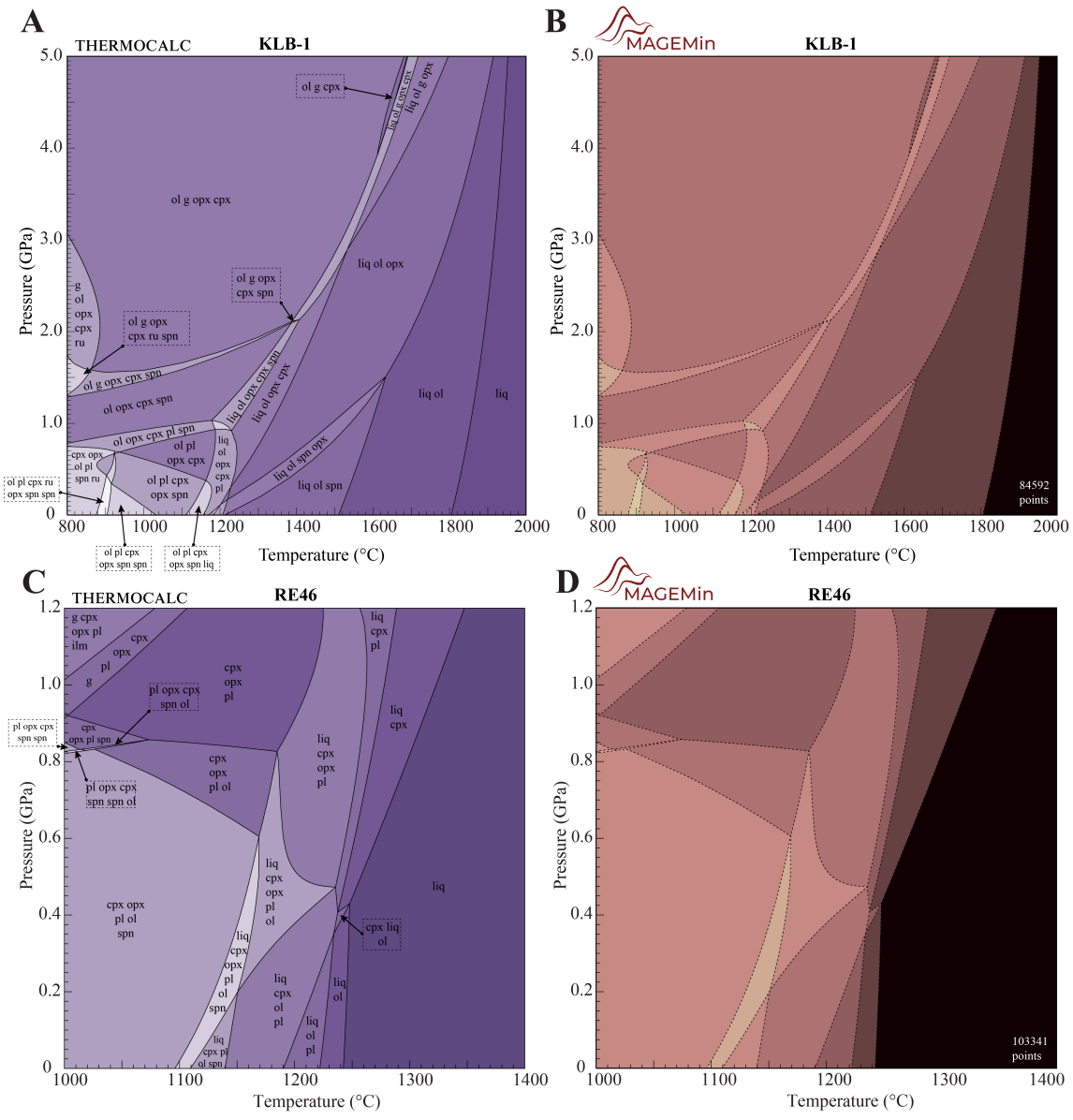

Figure 4. Comparison of dry pseudosections produced by THERMOCALC and MAGEMin. A, B, KLB-1 peridotite. C,D, RE46 Islandic basalt. For comparison, THERMOCALC reaction lines are shown as dashed lines in the MAGEMin pseudosection. Shading represents the variance of the system.

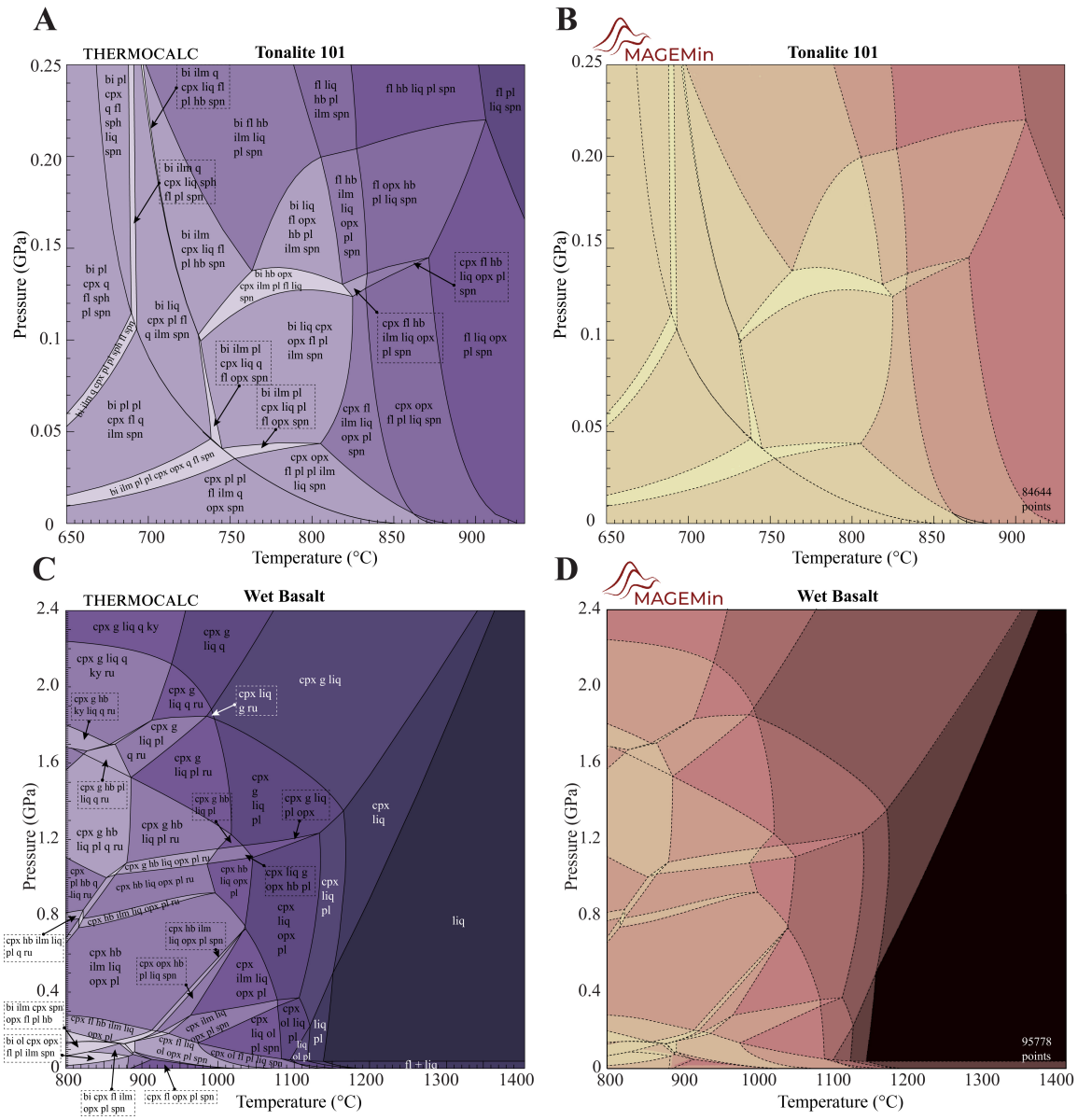

Figure 5. Comparison of wet pseudosections produced by THERMOCALC and MAGEMin. A, B, T101 tonalite. C,D, Wet basalt.

The pseudosections for N-MOR basalt and MIX1G pyroxenite were computed only with MAGEMin in the KNCFMASTOCr chemical system (Fig. 4A,B) from 0 to 1.2 GPa and from 500 to 1400 °C, and from 0 to 2.0 GPa and from 600 to 1600 °C, respectively.

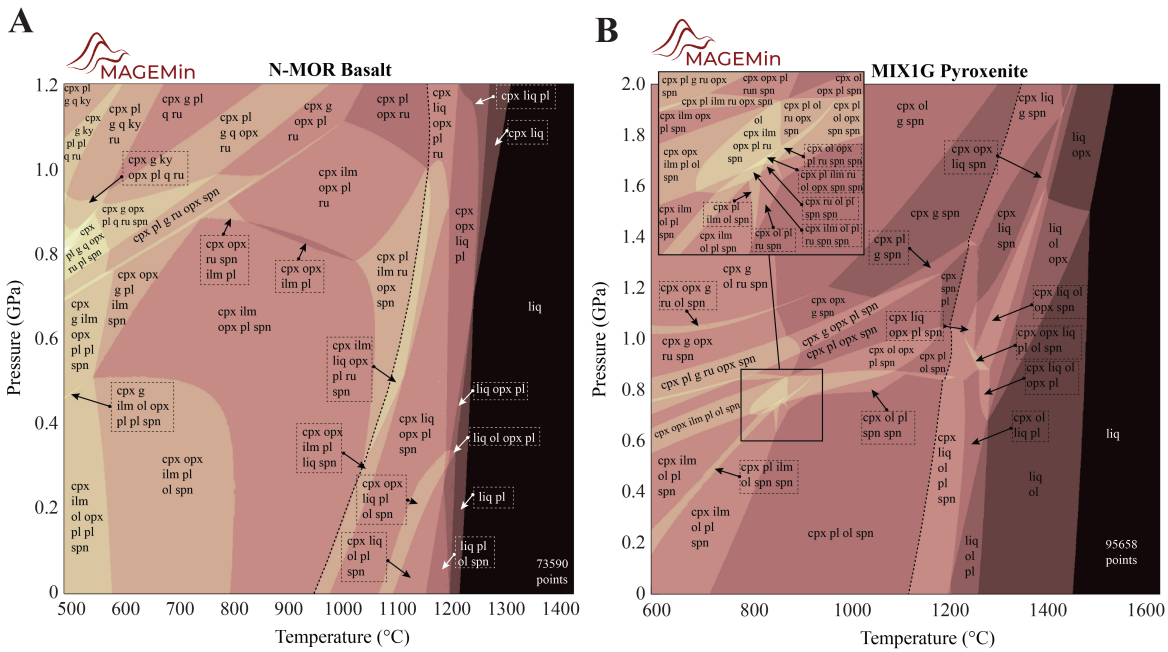

Figure 6. Pseudosections for N-MOR basalt and MIX1G pyroxenite.

4.2 Seismic velocities

Seismic velocities (see Fig. 7) are computed following the approach described in Connolly and Kerrick (2002) such as:

$$v_p = \sqrt{\frac{K_b + \frac{4K_s}{3}}{\rho}}, \tag{39}$$

and

$$v_s = \sqrt{\frac{K_s}{\rho}}, \tag{40}$$

where v_p is the P-wave velocity, v_s the S-wave velocity, ρ the density, K_b the adiabatic bulk modulus and K_s is the elastic shear modulus. The adiabatic bulk modulus is calculated from the thermodynamic data as

$$K_b = -\frac{\partial G_{sys}}{\partial P}\left[\frac{\partial^2 G_{sys}}{\partial P^2} + \left(\frac{\partial}{\partial P}\frac{\partial G_{sys}}{\partial T}\right)^2 \Big/ \frac{\partial^2 G_{sys}}{\partial T^2}\right]^{-1}. \tag{41}$$

Shear modulii cannot be computed from thermodynamic data, and are therefore calculated using an empirical relation (Connolly & Kerrick, 2002):

$$K_s = K_s^0 + T\frac{\partial K_s}{\partial T} + P\frac{\partial K_s}{\partial P}. \tag{42}$$

The shear modulii of the appropriate phases used in this study are taken from the database provided in Perple_X (Connolly, 2005). The database is a collection of shear modulii data mainly from Helffrich (1996), and from Karki et al. (2001), Sinogeikin et al. (2000), Bailey and Holloway (2000) and Bass et al. (1995). The bulk-rock seismic velocities are calculated without anelasticity correction, using a Voight–Reuss–Hill averaging of the velocities of the constituent phases, weighted by volume fraction (Connolly & Kerrick, 2002).

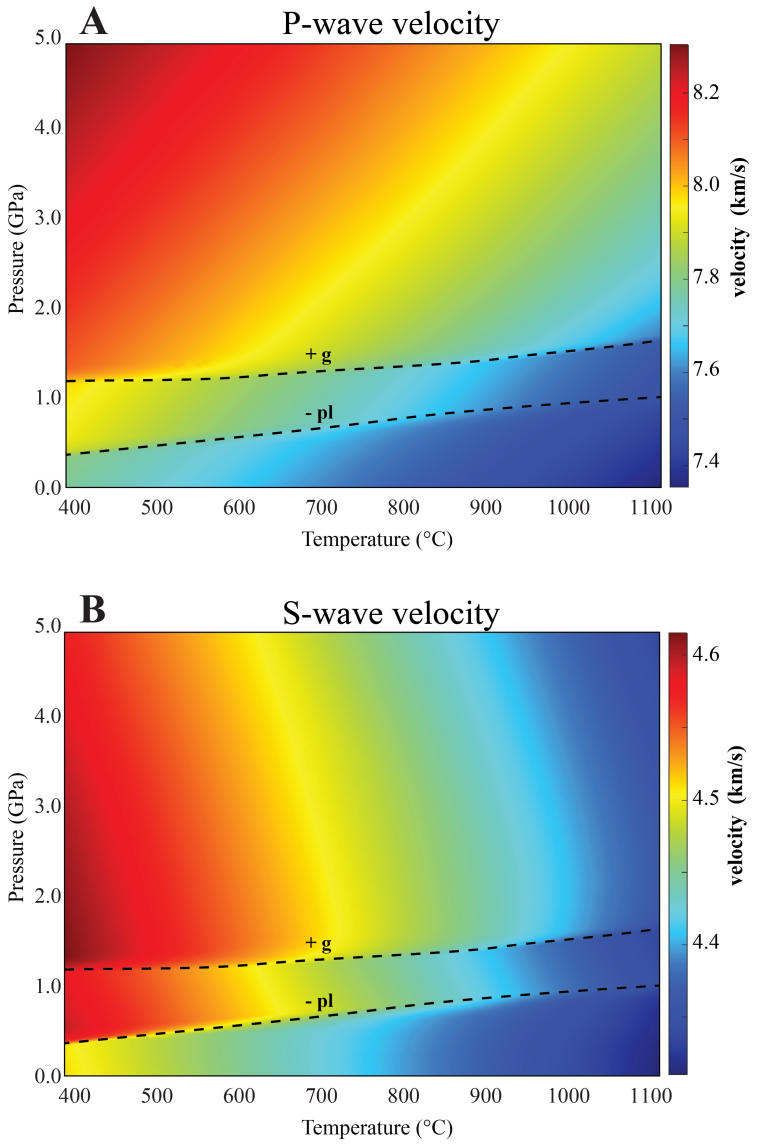

Figure 7. Example of seismic velocity computation for KLB-1 peridotite. A, P-wave velocity. B, S-wave velocity.

5 Discussion

5.1 Minimization approach

Here, we present a new Gibbs energy minimization approach applied to multiphase multicomponent systems. While some of the key ideas of our approach are based on the method of Partitioning Gibbs Energy (PGE) (e.g., Piro et al., 2013; Kruskopf & Visuri, 2017) we extended it to account for modelling of mineral solid solutions involving mixing-on-sites (Eq. 17 to 21). In Piro et al. (2013) the fraction of the end-members are updated using Eq. 15, whereas in our formulation the PGE stage is used to decrease the residual between $x_{i(\lambda)}$ and $p_{i(\lambda)}$. Essentially, the expression $\exp\left(-\frac{\Delta\mu_{i(\lambda)}}{RT}\right)$ of Eq. 21 forces the system to progressively satisfy the Gibbs Duhem rule by penalizing the fraction of end-members (hence, the mass constraint) computed during local minimization. However, to avoid divergence, the PGE stage requires a good initial guess, proper set of under-

relaxing factors and more critically, a highly consistent local minimization step. Although NLopt (Johnson, 2021) implements several gradient-based minimizers with inequality constraints (SLSQP, MMA, CCSAQ), we find that the CCSAQ algorithm (Svanberg, 2002) yields by far the best consistency and precision compared to SLSQP and linear MMA.

5.2 Consistency

The application of MAGEMin to the igneous thermodynamic dataset of Holland et al. (2018) shows very good agreement with pseudosections produced with THERMOCALC (Figs 3 and 4). However, minor differences can be observed in some regions. For instance the tonalite 101 pseudosection produced with MAGEMin (Fig. 4B) has an irregular reaction line at ca. 750 °C and 0.1 GPa (Fig. 3B). This is caused by oscillations when getting close to convergence, where a relaxed solution tolerance was accepted (tol $\leq 10^{-4}$ instead of the default value of 10^{-5}). Similar irregular reactions lines related to slightly relaxed tolerances can be observed in N-MOR basalt at ca. 750 °C and 0.88 GPa (Fig. 5A) and in MIX1G pyroxenite at ca. 1250 °C and 1.4 GPa (Fig. 5B).

5.3 Computational efficiency

Pseudosections presented in this work have been run in parallel on 6 logical processors on an Intel(R) Core(TM) i5-11400H. Single point calculation time has been averaged for each pseudosection which yielded 96 ms for KLB-1, 122 ms for RE46, 186 ms for Tonalite 101 and 162 ms for Wet Basalt. The large increase of calculation time for water-bearing compositions (Tonalite 101 and Wet Basalt) stems from having a larger number of discrete points during levelling (+ 40 ms) and a larger number of global iterations to reach convergence (+40 to 60 iterations on average).

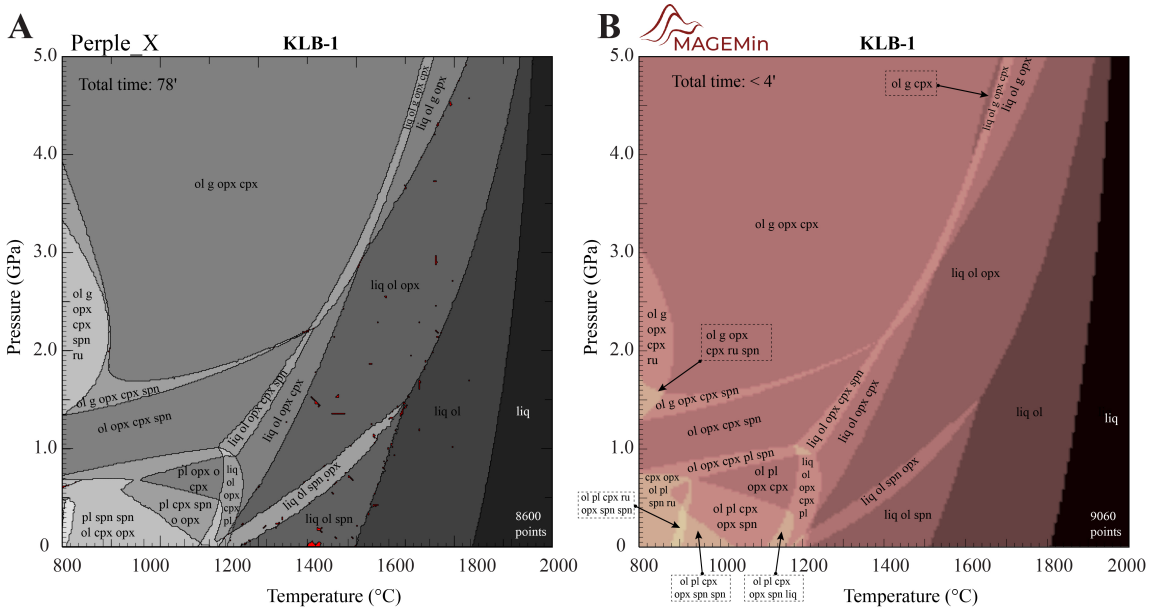

Figure 8. Comparison of KLB-1 pseudosections produced by Perple_X and MAGEMin. For the Perple_X pseudosection, we used version 6.9.1, the database file hp633ver.dat and the solution models Sp(HGP), Gt(HGP), Cpx(HGP), melt(HGP), O(HGP), Opx(HGP), feldspar and excluding "enL" and "fo8L". In order to have a better resolution of the reaction lines, we increased the exploratory and autorefine parameters to 60 and 200, respectively. For MAGEMin, we employed four levels of grid refinement in order to reach a similar number of minimization points as displayed in the Perple_X log.

In order to roughly compare our results with Perple_X (Connolly, 2005), we recomputed the KLB-1 pseudosection at similar resolution (±9000 grid points, Fig. 6). Although Perple_X did not include the last version of the dataset "hp634ver.dat" at the time we generated the diagram (Fig. 6A), we obtain a similar pseudosection nearly 20 times faster (Fig. 6B). Note that with default option the pseudosection was computed with Perple_X in 36 minutes, but the overall quality of the grid was quite degraded and we therefore choose to increase the grid resolution (exploratory and autorefine set to 60 and 200, respectively). In terms of single core performance, we still find that MAGEMin is nearly 3 times faster and yields cleaner diagrams with less visible artefacts (Fig. 6). Moreover, since the current version of Perple_X is not parallelized, the computational differences are more significant in practice. In the other comparable G-minimization software, Theriak and pMELTS, the Holland et al. (2018) thermodynamic dataset is not or cannot be implemented.

5.4 Coupling with geodynamic codes

In order to facilitate coupling with geodynamic codes we provide a Julia wrapper to MAGEMin. The Julia wrapper (called MAGEMin_C) allows the user to directly call the C functions of MAGEMin without writing data to disk first (which is slow). The results of the minimization are saved into a structure that is also accessed through the Julia interface. Here we provide a simple example.

Assuming Julia is installed, to install MAGEMin_C, first open a Julia terminal and type:

```
julia> ]                                        # opens the package manager
pkg> add MAGEMin_C                              # MAGEMin_C
```

To compute a phase equilibrium, first leave the package manager (using backspace) and enter the following commands:

```
julia> using MAGEMin_C                          # load MAGEMin_C package
julia> gv, DB      = init_MAGEMin();            # initializes MAGEMin
julia> P_kbar,T_C  = 8.0, 800.0;
julia> bulk_rock   = get_bulk_rock(gv, 0);# bulk-rock composition for test 0 (KLB-1 peridotite)
julia> gv.verbose  = -1;                        # switch off run-time verbose
julia> out         = point_wise_minimization(P_kbar,T_C, bulk_rock, gv, DB);
julia> print_info(out);                         # full display of the minimized point
```

A complete guide of the Julia interface is provided on the MAGEMin webpage.

5.5 Current limitations and known problems

Currently, only the thermodynamic dataset for igneous systems (Holland et al., 2018) has been implemented in MAGEMin. Yet, our approach is generally applicable and should thus in principle work with any thermodynamic dataset. In order to account for other petrological systems, additional datasets could be implemented for example relevant to metapelitic (R. W. White et al., 2014) or metabasitic systems (Green et al., 2016). We expect the performance of those cases to be at least as good, as the equations of state for solution phases are somewhat simpler.

To be successful, our implementation of the Partitioning Gibbs Energy method heavily relies on having a good initial guesses, here provided by the levelling stage. At present, our approach tends to have difficulties to converge in some cases, mainly at sub-solidus conditions and for water-bearing bulk-rock compositions (< 650 °C). When divergence is observed, it usually occurs very fast and several methods are being tested to remedy that issue. One potential cause of divergence can be attributed to the current discretization approach employed during the levelling stage. Indeed, for complex solution phases, such as amphibole, the large discretization step used to keep the number of pseudocompounds relatively low (< 6000) can be a source of uneven sampling of the solution phase space, which may lead to minimization failure (likely because the minimization gets stuck in an unfeasible local minimum). A possible workaround would be to add the complete list of end-members bounding the space of valid site-occupancies, following the procedure described in Myhill and Connolly (2021). A complementary option could be to precompute over a given P-T range the local minima of each solution phase and add them to the pseudocompound list.

Finally, magemin does not presently account for bulk-rock compositions that are in a different system from the set of solution phase models (equations of state) provided in Holland et al. (2018). While TiO_2, Fe_2O_3, Cr_2O_3 and H_2O can somewhat be set to 0.0, other system components cannot be ignored without reformulating some of solution phase model. However, being able to obtain stable phase equilibria in restricted chemical system is crucial to model magmatic differentiation. As a consequence we are actively working on producing a generalized set of solution phase models accounting for reduced chemical systems.

6 Conclusions

We present a new parallel Gibbs energy minimizer that allows us to compute stable equilibria in complex multicomponent multiphase systems. We successfully extended the Partitioning Gibbs Energy approach to Gibbs energy functions that model mixing-

on-sites, and applied it to the most recent thermodynamic igneous dataset. Pseudosection computation shows very consistent results with THERMOCALC and improved performance with respect to other software such as the current Perple_X version. The parallel design of MAGEMin makes it highly scalable on multicore machines. While in this contribution we computed pseudosections using a MATLAB-based interface, MAGEMin has been developed with the objective to provide the community with a minimization package easily callable from any geodynamic codes. Such tool can also potentially provide a robust framework for thermodynamic database inversions.

7 Software availability

A complete guide on how to download, install and run MAGEMin is given in the git repository https://github.com/ComputationalThermodynamics/MAGEMin.git. The version of the code is also made available on Zenodo, doi:10.5281/zenodo.6347567

Acknowledgments

This study was funded by the European Research Council through the MAGMA project, ERC Consolidator Grant #771143. We greatly thank Roger Powell for help with producing the THERMOCALC pseudosections presented in this study. We thank Markus Bachmayr for help with consistent discretization of the G-surfaces of solution phases and James Connolly for comments on the manuscript. We also thank the anonymous reviewer for suggestions and Robert Myhill for his review which greatly helped to clarify the manuscript and for valuable github contributions to MAGEMin.

Appendix A Equations of state in the example thermodynamic dataset

Here we summarize how the equations of state are formulated in our example thermodynamic dataset, that of Holland et al. (2018). We detail the information passed as input to both THERMOCALC and MAGEMin, using the Holland et al. (2018) equation of state for the olivine solid solution as an example. In Appendix B, we show how MAGEMin sets up the minimization step for the model olivine solid solution.

In Holland et al. (2018), and related thermodynamic datasets such as R. W. White et al. (2014) and Green et al. (2016), the equation of state of a mineral is assembled from up to four components (for a pure phase, consisting of a single end-member, only aspects 2 or 3 apply):

1. A choice about what composition space the model solution phase should encompass, which discrete mixing sites should be distinguished, and which ions should be considered to mix on each site; e.g. Table A1. These choices determine which end-members will be required.
2. The $G(P,T)$ relations for those model end-members that are found in the appropriate version of the Holland and Powell (2011) internally-consistent dataset of thermodynamic properties of end-members (IDE).
3. $G(P,T)$ relations for those model end-members that are not in the IDE. For non-IDE end-member i, this is constructed from the $G(P,T)$ curves of a subset of Λ IDE end-members, as $G_i(P,T) = \Sigma_{\lambda=1}^{\Lambda} \nu_\lambda G_\lambda(P,T) + a + bT + cP$, where a, b and c are constants, and the net composition of the combination of end-members Λ yields the composition of i. The IDE end-members Λ do not necessarily appear anywhere else in the thermodynamic dataset.
4. Activity–composition (a–x) relations, which describe the thermodynamic contributions of mixing among the end-members. In general these follow the asymmetric formalism of Holland and Powell (2003). In the asymmetric formalism, the configurational entropy is formulated in terms of mixing on sites, potentially with a

non-unity scaling factor applied to each site as described below. The non-ideal mixing contribution from each end-member is defined in terms of a single interaction energy (Margules parameter, W) between each pair of end-members (equation A20), which may be asymmetric, and may be linearly dependent on P and/or T (thereby potentially contributing excess volume and/or entropy terms in addition to excess enthalpy).

In the Holland et al. (2018) model for the olivine solution, the end-members and mixing site occupancies are as shown in Table A1.

Table A1. End-members and mixing site occupancies of olivine in the Holland et al. (2018) thermodynamic dataset.

End-member	Abbreviation	Formula	Mixing sites				
			M1		M2		
			Mg	Fe	Mg	Fe	Ca
forsterite	fo	Mg_2SiO_4	1	0	1	0	0
fayalite	fa	Fe_2SiO_4	0	1	0	1	0
ordered intermediate	cfm	$MgFeSiO_4$	1	0	0	1	0
monticellite	mont	$CaMgSiO_4$	1	0	0	0	1

The end-members forsterite, fayalite and monticellite are taken directly from the IDE. End-member cfm represents full ordering of Mg and Fe on the M1 and M2 sites; it is not in the IDE, but the $G_{\rm cfm}(P,T)$ curve is formed from

$$G_{\rm cfm}(P,T) = 1/2(G_{\rm fo}(P,T) + G_{\rm fa}(P,T)) + \Delta G^{od}_{\rm cfm} \tag{A1}$$

where $\Delta G^{od}_{\rm cfm}$ is the Gibbs energy of ordering in the cfm composition, and has the form $a + bT + cP$.

Compositional and order variability within the solid solution are defined in terms of site fractions:

$$\begin{aligned} x &= (x{\rm FeM1} + x{\rm FeM2})/(x{\rm FeM1} + x{\rm FeM2} + x{\rm MgM1} + x{\rm MgM2}) && \text{(A2)}\\ c &= x{\rm CaM2} && \text{(A3)}\\ Q &= x - x{\rm FeM1}/(x{\rm FeM1} + x{\rm MgM1}) && \text{(A4)} \end{aligned}$$

where, for example, xFeM1 is the fraction of Fe on the M1 site. Compositional and order variables are subject to bounds, which for x, c and Q, as in most cases, are [0.0 1.0]. The variables are chosen so as to ensure that the fraction of mixing ions on each site are normalised to a constant total, and, if relevant, that charge balance is obeyed within the mineral.

Written in these variables, the site fractions are expressed as

$$x{\rm MgM1} = 1 + Q - x, \tag{A5}$$

$$x{\rm FeM1} = -Q + x, \tag{A6}$$

$$x{\rm MgM2} = 1 - c - Q - x + cx, \tag{A7}$$

$$x{\rm FeM2} = Q + x + (-c)x, \tag{A8}$$

$$x{\rm CaM2} = c, \tag{A9}$$

The site fraction expressions are required to express the ideal activity, and hence the configurational entropy, of the model end-members in the solution. For some minerals, though not in olivine, the entropic contribution of a particular site is reduced by a scaling factor (see e.g. Holland et al., 2021), to simulate the effects of short-range order in the crystal structure. Thus, the ideal activity of end-member i can be expressed as

$$a^{id}_{i(\lambda)} = c_i \prod_s (X^s_{e_{s,i}})^{\nu_s f_s} \tag{A10}$$

where $X^s_{e_{s,i}}$ is the site fraction of the element $e_{s,i}$ that appears on site s, ν_s is the number of atoms mixing on s, c_i the normalisation constant to give $a^{id}_{i(\lambda)} = 1$ for pure i, and f the scaling factor for the site. For olivine ($f = 1$ for all sites), the ideal activities are

$$a^{id}_{\text{mont}} = x\text{MgM1} \cdot x\text{CaM2}, \tag{A11}$$

$$a^{id}_{\text{fa}} = x\text{FeM1} \cdot x\text{FeM2}, \tag{A12}$$

$$a^{id}_{\text{fo}} = x\text{MgM1} \cdot x\text{MgM2}, \tag{A13}$$

$$a^{id}_{\text{cfm}} = x\text{MgM1} \cdot x\text{FeM2}. \tag{A14}$$

The proportions of the end-members present at a given composition and state of order can be expressed as:

$$p_{\text{mont}} = c, \tag{A15}$$

$$p_{\text{fa}} = -Q + x, \tag{A16}$$

$$p_{\text{fo}} = 1 - c - Q - x + cx, \tag{A17}$$

$$p_{\text{cfm}} = 2Q + (-c)x. \tag{A18}$$

The equation of state is conveniently assembled in terms of the $\mu_i(P, T, \mathbf{x}, \mathbf{Q})$, where μ_i is the chemical potential of end-member i, and $\mu_i = \frac{\partial G_i}{\partial p_i}$. μ_i can be written as

$$\mu_i = \mu^0_i + RT \log(a^{id}_i) + \mu^{ex}_i, \tag{A19}$$

where μ^0_i is the chemical potential of pure i, with $\mu^0_i(P, T) = G_i(P, T)$, as described above. In the asymmetric formalism, μ^{ex}_i is given by

$$\mu^{ex}_i = -\sum_{m=1}^{N_{ol}-1} \sum_{n>m}^{N_{ol}} (\phi'_m - \phi_m)(\phi'_n - \phi_n) W_{m,n} \left(\frac{2v_i}{v_m + v_n} \right). \tag{A20}$$

Here, ϕ_i is the proportion of end-member i weighted by the asymmetry parameters, as $\phi_i = (p_i v_i)/(\sum_{m=1}^{N_{ol}} p_m v_m)$, with v_i the asymmetry parameter for end-member i. ϕ'_m is the value of ϕ_m in end-member i, such that $\phi'_m = 1$ where $m = i$ and $\phi'_m = 0$ where $m \neq i$. $W_{m,n}$ is the interaction energy between end-members m and n in the solution. The values of model parameters in the olivine solid solution are given in Table A2.

Table A2. Values of parameters in the model olivine solid solution of Holland et al. (2018)

$W_{m,n}$ binary	value
W(mont,fa)	24 kJ
W(mont,fo)	38 kJ
W(mont,cfm)	24 kJ
W(fa,fo)	9 kJ
W(fa,cfm)	4.5 kJ
W(fo,cfm)	4.5 kJ
v_{fo}	1
v_{fa}	1
v_{cfm}	1
v_{mont}	1
$\Delta G^{od,a}_{\mathrm{cfm}}$	0 kJ
$\Delta G^{od,b}_{\mathrm{cfm}}$	0 kJ/K
$\Delta G^{od,c}_{\mathrm{cfm}}$	0 kJ/kbar

Appendix B Implementation in MAGEMin

MAGEMin uses the input outlined in Appendix A to assemble the Gibbs energy of olivine at pressure P and temperature T:

$$G_{ol}(\mathbf{x},\mathbf{Q})|_{P,T} = \sum_{i=1}^{N_{ol}} \left(\mu_{i(ol)}(\mathbf{x},\mathbf{Q}) \cdot p_{i(ol)}(\mathbf{x},\mathbf{Q})\right)|_{P,T}, \tag{B1}$$

where $\mu_{i(ol)}$ is obtained as in equation A20. Equation B1 constitutes the objective function for the minimization step. The gradient of the objective function is the derivative of the Gibbs from energy of olivine with respect to the compositional variables:

$$\frac{\partial G_{ol}}{\partial x_k} = \sum_{i=1}^{N_{ol}} \mu_{i(ol)} \frac{\partial p_{i(ol)}}{\partial x_k}, \tag{B2}$$

where $\frac{\partial p_{i(ol)}}{\partial x_k}$ is given in Table B1.

Table B1. Partial derivatives of end-member proportions as function of compositional variables

	$\frac{\partial p_i}{\partial x}$	$\frac{\partial p_i}{\partial c}$	$\frac{\partial p_i}{\partial Q}$
$\frac{\partial p_{fo}}{\partial x_k}$	c-1	x-1	-1
$\frac{\partial p_{fa}}{\partial x_k}$	1	0	-1
$\frac{\partial p_{cfm}}{\partial x_k}$	-c	-x	2
$\frac{\partial p_{mont}}{\partial x_k}$	0	1	0

During the minimization, the value of all site fractions is required to be ≥ 0 via a set of non-linear inequality constraints (derived from Eqs. A5 to A9) that is passed to the local minimizer. The gradients of the site-fractions with respect to the compositional and order variables are given in Table B2.

Table B2. Partial derivatives of site-fractions as function of compositional variables

	$\frac{\partial sf_i}{\partial x}$	$\frac{\partial sf_i}{\partial c}$	$\frac{\partial sf_i}{\partial Q}$
$\frac{\partial xMgM1}{\partial x_k}$	-1	0	1
$\frac{\partial xFeM1}{\partial x_k}$	1	0	-1
$\frac{\partial xMgM2}{\partial x_k}$	c-1	x-1	-1
$\frac{\partial xFeM2}{\partial x_k}$	$1-c$	x	1
$\frac{\partial xCaM2}{\partial x_k}$	0	1	0

The above expressions are passed to NLopt (Johnson, 2021) together with an initial guess for the compositional variables. Subsequently, the objective function is minimized using the CCSAQ algorithm (Svanberg, 2002).

References

Asimow, P. D., & Ghiorso, M. S. (1998). Algorithmic modifications extending melts to calculate subsolidus phase relations. *American Mineralogist*, *83*(9-10), 1127-1132. doi: doi:10.2138/am-1998-9-1022

Bailey, E., & Holloway, J. R. (2000). Experimental determination of elastic properties of talc to 800 c, 0.5 gpa; calculations of the effect on hydrated peridotite, and implications for cold subduction zones. *Earth and Planetary Science Letters*, *183*(3-4), 487–498.

Bass, J. D., et al. (1995). Elasticity of minerals, glasses, and melts. *Mineral physics and crystallography: A handbook of physical constants*, *2*, 45–63.

Berman, R. G. (1991). Thermobarometry using multi-equilibrium calculations; a new technique, with petrological applications. *The Canadian Mineralogist*, *29*(4), 833–855.

Bezanson, J., Edelman, A., Karpinski, S., & Shah, V. B. (2017). Julia: A fresh approach to numerical computing. *SIAM review*, *59*(1), 65–98.

Burgos-Solórzano, G. I., Brennecke, J. F., & Stadtherr, M. A. (2004). Validated computing approach for high-pressure chemical and multiphase equilibrium. *Fluid Phase Equilibria*, *219*(2), 245-255. doi: https://doi.org/10.1016/j.fluid.2003.12.013

Çetin, G., & Keçebaş, A. (2021). Optimization of thermodynamic performance with simulated annealing algorithm: A geothermal power plant. *Renewable Energy*, *172*, 968-982. doi: https://doi.org/10.1016/j.renene.2021.03.101

Connolly, J., & Kerrick, D. (2002). Metamorphic controls on seismic velocity of subducted oceanic crust at 100–250 km depth. *Earth and Planetary Science Letters*, *204*(1-2), 61–74.

Connolly, J. A. D. (1990). Multivariable phase diagrams; an algorithm based on generalized thermodynamics. *American Journal of Science*, *290*(6), 666-718. doi: 10.2475/ajs.290.6.666

Connolly, J. A. D. (2005). Computation of phase equilibria by linear programming: A tool for geodynamic modeling and its application to subduction zone decarbonation. *Earth and Planetary Science Letters*, *236*, 524-541.

Connolly, J. A. D. (2017). A primer in gibbs energy minimization for geophysicists. *Petrology*, *25*, 526-534.

Dantzig, G. B. (1963). *Linear programming and extensions.* Princeton, N.J.: Princeton University Press.

de Capitani, C., & Brown, T. H. (1987). The computation of chemical equilibrium in complex systems containing non-ideal solutions. *Geochimica et Cosmochim-*

ica Acta, *51*(10), 2639-2652. doi: https://doi.org/10.1016/0016-7037(87)90145-1

de Capitani, C., & Petrakakis, K. (2010). The computation of equilibrium assemblage diagrams with theriak/domino software. *American Mineralogist*, *95*(7), 1006-1016. doi: doi:10.2138/am.2010.3354

Fateen, S.-E. K. (2016, nov). Unconstrained gibbs minimization for solving multi-reaction chemical equilibria using a stochastic global optimizer. *Comput. Appl. Eng. Educ.*, *24*(6), 899–904. doi: 10.1002/cae.21759

Feppon, F., Allaire, G., & Dapogny, C. (2020). Null space gradient flows for constrained optimization with applications to shape optimization. *ESAIM: COCV*, *26*, 90. doi: 10.1051/cocv/2020015

Gale, A., Dalton, C. A., Langmuir, C. H., Su, Y., & Schilling, J.-G. (2013). The mean composition of ocean ridge basalts. *Geochemistry, Geophysics, Geosystems*, *14*(3), 489-518. doi: https://doi.org/10.1029/2012GC004334

Ganguly, J. (2001). Thermodynamic modelling of solid solutions. *EMU Notes in Mineralogy*, *3*(3), 37–69.

Gasparik, T. (2014). System cao–mgo–sio 2. In *Phase diagrams for geoscientists* (pp. 81–129). Springer.

Ghiorso, M. S. (1983). Lseqieq: a fortran iv subroutine package for the analysis of multiple linear regression problems with possibly deficient pseudorank and linear equality and inequality constraints. *Computers & Geosciences*, *9*, 391-416.

Ghiorso, M. S. (1985). Chemical mass transfer in magmatic processes. *Contributions to Mineralogy and Petrology*, *90*, 107-120.

Ghiorso, M. S., & Sack, R. O. (1995). Chemical mass transfer in magmatic processes iv. a revised and internally consistent thermodynamic model for the interpolation and extrapolation of liquid-solid equilibria in magmatic systems at elevated temperatures and pressures. *Contributions to Mineralogy and Petrology*, *119*(2/3), 197-212.

Gibbs, J. W. (1878). On the equilibrium of heterogeneous substances. *American Journal of Science*, *3*(96), 441–458.

Green, E. C. R., White, R. W., Diener, J. F. A., Powell, R., Holland, T. J. B., & Palin, R. M. (2016). Activity–composition relations for the calculation of partial melting equilibria in metabasic rocks. *Journal of Metamorphic Geology*, *34*(9), 845-869. doi: https://doi.org/10.1111/jmg.12211

Helffrich, G. (1996). Subducted lithospheric slab velocity structure: Observations and mineralogical inferences. *Washington DC American Geophysical Union Geophysical Monograph Series*, *96*, 215–222.

Helgeson, H. C. (1978). Summary and critique of the thermodynamic properties of rock-forming minerals. *American Journal of Science*, *278*, 1–229.

Hirschmann, M. M., Kogiso, T., Baker, M. B., & Stolper, E. M. (2003, 06). Alkalic magmas generated by partial melting of garnet pyroxenite. *Geology*, *31*(6), 481-484. doi: 10.1130/0091-7613(2003)031⟨0481:AMGBPM⟩2.0.CO;2

Holland, T., & Powell, R. (2003). Activity–composition relations for phases in petrological calculations: an asymmetric multicomponent formulation. *Contributions to Mineralogy and Petrology*, *145*(4), 492–501.

Holland, T., & Powell, R. (2011). An improved and extended internally consistent thermodynamic dataset for phases of petrological interest, involving a new equation of state for solids. *Journal of metamorphic Geology*, *29*(3), 333–383.

Holland, T. J. B., Green, E. C. R., & Powell, R. (2018). Melting of peridotites through to granites: a simple thermodynamic model in the system kncfmashtocr. *Journal of Petrology*, *59*(5), 881–900.

Holland, T. J. B., Green, E. C. R., & Powell, R. (2021). A thermodynamic model for feldspars in KAlSi3O8-NaAlSi3O8-CaAl2Si2O8 for mineral equilibrium calculations. *Journal of Metamorphic Geology*, *n/a*(n/a). doi: https://doi.org/10.1111/jmg.12639

Holland, T. J. B., & Powell, R. (1998). An internally consistent thermodynamic data set for phases of petrological interest. *Journal of Metamorphic Geology*, *16*(3), 309-343. doi: https://doi.org/10.1111/j.1525-1314.1998.00140.x

Hou, T., Botcharnikov, R., Moulas, E., Just, T., Berndt, J., Koepke, J., ... Holtz, F. (2021, 01). Kinetics of fe–ti oxide re-equilibration in magmatic systems: Implications for thermo-oxybarometry. *Journal of Petrology*, *61*(11-12). (egaa116) doi: 10.1093/petrology/egaa116

Johnson, S. G. (2021). *The nlopt nonlinear-optimization package* [Software]. Retrieved from `http://github.com/stevengj/nlopt` doi: 10.7283/633E-1497

Karki, B. B., Stixrude, L., & Wentzcovitch, R. M. (2001). High-pressure elastic properties of major materials of earth's mantle from first principles. *Reviews of Geophysics*, *39*(4), 507–534.

Katz, R. F., Jones, D. W. R., Rudge, J. F., & Keller, T. (2022). Physics of melt extraction from the mantle: Speed and style. *Annual Review of Earth and Planetary Sciences*, *50*.

Keller, T., & Katz, R. F. (2016). The Role of Volatiles in Reactive Melt Transport in the Asthenosphere. *Journal of Petrology*, *57*(6), 1073-1108. doi: 10.1093/petrology/egw030

Keller, T., Katz, R. F., & Hirschmann, M. M. (2017). Volatiles beneath mid-ocean ridges: Deep melting, channelised transport, focusing, and metasomatism. *Earth and Planetary Science Letters*, *464*, 55–68.

Keller, T., May, D. A., & Kaus, B. J. P. (2013). Numerical modelling of magma dynamics coupled to tectonic deformation of lithosphere and crust. *Geophysical Journal International*, *195*(3), 1406-1442. doi: 10.1093/gji/ggt306

Keller, T., & Suckale, J. (2019). A continuum model of multi-phase reactive transport in igneous systems. *Geophysical Journal International*, *219*(1), 185-222. doi: 10.1093/gji/ggz287

Kruskopf, A., & Visuri, V.-V. (2017). A gibbs energy minimization approach for modeling of chemical reactions in a basic oxygen furnace. *Metallurgical and Materials Transactions B*, *48*(6). doi: 10.1007/S11663-017-1074-X

Lanari, P., & Duesterhoeft, E. (2018, 11). Modeling Metamorphic Rocks Using Equilibrium Thermodynamics and Internally Consistent Databases: Past Achievements, Problems and Perspectives. *Journal of Petrology*, *60*(1), 19-56. doi: 10.1093/petrology/egy105

Lasaga, A. C. (1986). Metamorphic reaction rate laws and development of isograds. *Mineralogical Magazine*, *50*(357), 359–373. doi: 10.1180/minmag.1986.050.357.02

Lothenbach, B., Kulik, D. A., Matschei, T., Balonis, M., Baquerizo, L., Dilnesa, B., ... Myers, R. J. (2019). Cemdata18: A chemical thermodynamic database for hydrated portland cements and alkali-activated materials. *Cement and Concrete Research*, *115*, 472-506. doi: https://doi.org/10.1016/j.cemconres.2018.04.018

Myhill, R., & Connolly, J. A. (2021). Notes on the creation and manipulation of solid solution models. *Contributions to Mineralogy and Petrology*, *176*(10), 1–19.

Pauken, M. (2011). *Thermodynamics for dummies*. John Wiley & Sons.

Piro, M., Banfield, J., Clarno, K., Simunovic, S., Besmann, T., Lewis, B., & Thompson, W. (2013). Coupled thermochemical, isotopic evolution and heat transfer simulations in highly irradiated uo2 nuclear fuel. *Journal of Nuclear Materials*, *441*(1), 240-251. doi: https://doi.org/10.1016/j.jnucmat.2013.05.060

Piro, M., & Simunovic, S. (2016). Global optimization algorithms to compute thermodynamic equilibria in large complex systems with performance considerations. *Computational Materials Science*, *118*, 87-96. doi: https://doi.org/10.1016/j.commatsci.2016.02.043

Piro, M. H. A. (2011). *Computation of Thermodynamic Equilibria Pertinent to*

Nuclear Materials in Multi-Physics Codes (Unpublished doctoral dissertation). Royal Military College of Canada (Canada).

Piro, M. H. A., Simunovic, S., Besmann, T. M., Lewis, B. J., & Thompson, W. T. (2013). The thermochemistry library thermochimica. *Computational Materials Science*, *67*.

Piwinskii, A. J. (1968). Experimental studies of igneous rock series central sierra nevada batholith, california. *The Journal of Geology*, *76*(5), 548-570. doi: 10.1086/627359

Powell, R. (1978). *Equilibrium thermodynamics in petrology: an introduction*. Harper & Row.

Powell, R., & Holland, T. (1988). An internally consistent dataset with uncertainties and correlations: 3. applications to geobarometry, worked examples and a computer program. *Journal of metamorphic Geology*, *6*(2), 173–204.

Powell, R., & Holland, T. (1993). On the formulation of simple mixing models for complex phases. *American Mineralogist*, *78*(11-12), 1174–1180.

Rummel, L., Kaus, B. J. P., Baumann, T. S., White, R. W., & Riel, N. (2020). Insights into the Compositional Evolution of Crustal Magmatic Systems from Coupled Petrological-Geodynamical Models. *Journal of Petrology*, *61*(2). doi: 10.1093/petrology/egaa029

Sinogeikin, S. V., Schilling, F. R., & Bass, J. D. (2000). Single crystal elasticity of lawsonite. *American Mineralogist*, *85*(11-12), 1834–1837.

Spear, F. S. (1988). The Gibbs method and Duhem's theorem: The quantitative relationships among P, T, chemical potential, phase composition and reaction progress in igneous and metamorphic systems. *Contributions to Mineralogy and Petrology*, *99*(2), 249-256. doi: 10.1007/BF00371465

Spear, F. S. (1993). Metamorphic phase equilibria and pressure-temperature-time paths. *Mineralogical Society of America Monograph*, 352–356.

Stixrude, L., & Lithgow-Bertelloni, C. (2011). Thermodynamics of mantle minerals - ii. phase equilibria. *Geophysical Journal International*, *184*(3), 1180-1213. doi: 10.1111/j.1365-246X.2010.04890.x

Stixrude, L., & Lithgow-Bertelloni, C. (2021, 09). Thermal expansivity, heat capacity and bulk modulus of the mantle. *Geophysical Journal International*, *228*(2), 1119-1149. Retrieved from `https://doi.org/10.1093/gji/ggab394` doi: 10.1093/gji/ggab394

Svanberg, K. (2002). A class of globally convergent optimization methods based on conservative convex separable approximations. *SIAM Journal on Optimization*, 555-573.

Takahashi, E. (1986). Melting of a dry peridotite klb-1 up to 14 gpa: Implications on the origin of peridotitic upper mantle. *Journal of Geophysical Research: Solid Earth*, *91*(B9), 9367-9382. doi: https://doi.org/10.1029/JB091iB09p09367

Taylor-West, J., & Katz, R. F. (2015). Melt-preferred orientation, anisotropic permeability and melt-band formation in a deforming, partially molten aggregate. *Geophysical Journal International*, *203*(2), 1253–1262.

Teh, Y., & Rangaiah, G. (2002). A study of equation-solving and gibbs free energy minimization methods for phase equilibrium calculations. *Chemical Engineering Research and Design*, *80*(7), 745-759. doi: https://doi.org/10.1205/026387602320776821

Tomlinson, E. L., & Holland, T. J. (2021). A thermodynamic model for the subsolidus evolution and melting of peridotite. *Journal of Petrology*, *62*(1), egab012.

Turner, A. J., Katz, R. F., Behn, M. D., & Keller, T. (2017). Magmatic focusing to mid-ocean ridges: The role of grain-size variability and non-newtonian viscosity. *Geochemistry, Geophysics, Geosystems*, *18*(12), 4342–4355.

White, R. W., Powell, R., Holland, T. J. B., Johnson, T. E., & Green, E. C. R.

(2014). New mineral activity–composition relations for thermodynamic calculations in metapelitic systems. *Journal of Metamorphic Geology*, *32*(3), 261-286. doi: https://doi.org/10.1111/jmg.12071

White, W., S.M., J., & G.B., D. (1958). Chemical equilibrium in complex mixtures. *Journal of Chemical Physics*, *28*, 751-755.

Xiang, H., & Connolly, J. A. D. (2021). Geops: An interactive visual computing tool for thermodynamic modelling of phase equilibria. *Journal of Metamorphic Geology*, *n/a*(n/a). doi: https://doi.org/10.1111/jmg.12626

Yang, H.-J., Kinzler, R. J., & Grove, T. L. (1996). Experiments and models of anhydrous, basaltic olivine-plagioclase-augite saturated melts from 0.001 to 10 kbar. *Contributions to Mineralogy and Petrology*, *124*, 1-18.

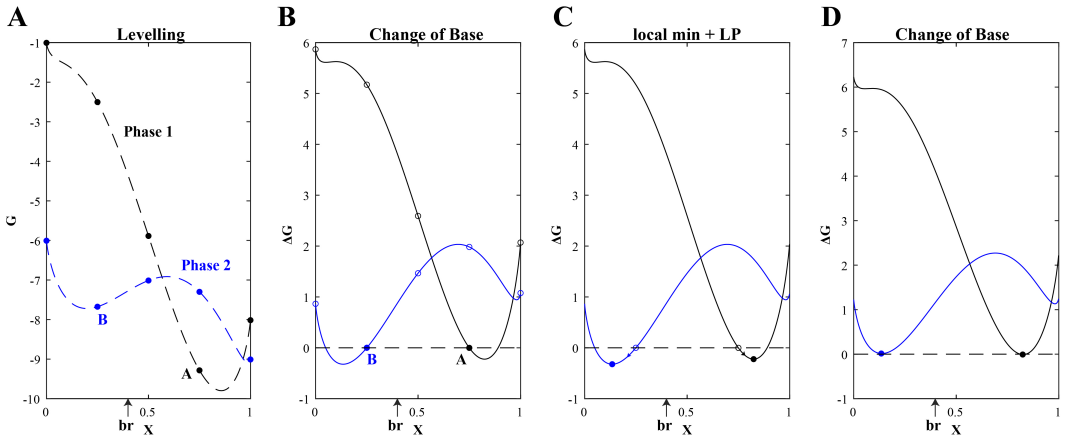

Figure 1. Simplified illustration of the minimization strategy, at pressure P=0 GPa and temperature T=1 K, with two solution phases λ_1 and λ_2 (modified after de Capitani and Brown (1987)). Both solution phases include 2 end-members of identical composition C=[1 0; 0 1] (at coordinate X=0.0 and X=1.0). The Gibbs energy of reference of the end-members are: $G0_{i1}^{\lambda 1}$ = -1.0, $G0_{i2}^{\lambda 1}$ = -8.0, $G0_{i1}^{\lambda 2}$ = -6.0 and $G0_{i2}^{\lambda 2}$ = -9.0. The ideal mixing terms are formulated as $RT\log(x)$ with R = 8.134 J/mol/K and T = 1.0 K. The excess terms are calculated as $G_{\rm ex}^{\lambda 1} = 35.0x_1^2x_2$ and $G_{\rm ex}^{\lambda 2} = 35.0x_1x_2^2{+}15.0x_1^2x_2$. The total Gibbs energy of each phase is expressed as $G^{\lambda} = \sum_{i=1}^{N_\lambda} x_i\mu_{i(\lambda)} = \sum_{i=1}^{N_\lambda} x_i\left(G0_i + RT\log(x_i) + G_{\rm ex}\right)$. A) During the levelling stage the G^{λ} function of each phase is discretized in composition space with a step of 0.25. Then, linear programming is used to find the combination of discrete points minimizing the Gibbs energy of the system $G_{\rm sys} = G^{\lambda 1} + G^{\lambda 2}$ while satisfying the mass constraint br = [0.6 0.4], here resulting in points A (α=0.7) and B (α=0.3). The Gibbs-hyperplane passing through discrete phases A and B is computed by solving $\Gamma_j = \mathbf{A}^{-1}b$, where $\mathbf{A}$ is the stoichiometry matrix ([0.25 0.75; 0.75 0.25]) and b is the vector of Gibbs energy of discrete points A and B ([-9.2846; -7.6753]). B) The whole system is rotated by recalculating the Gibbs energy curves G^{λ} as ΔG^{λ} = $\sum_{i=1}^{N_\lambda} x_i\left(G0_i - \sum_{j=1}^{C}\Gamma_j a_{ij} + RT\log(x_i) + G_{\rm ex}\right)$, where Γ_j = [-6.8706; -10.0893] and a_i is the compositional vector of end-member i. This step effectively levels the plane passing through points A and B to the horizontal i.e., $\Delta G^{\lambda A,B}$ = 0.0. C) Starting from discrete points A and B (empty black and blue circles) a gradient-based method is used to find the minimum of phases λ_1 and λ_2 (X_1 = 0.8242 and X_2 = 0.1345). D) Using the minimized points the Gibbs plane is rotated again ($\Delta\Gamma_j$ = [-0.3631; -0.1806], Γ_j=Γ_j + $\Delta\Gamma_j$) and for this simplified case-study, the system is considered to have converged, as there are no phases left for which ΔG<0. The phase fractions are retrieved as $\alpha_{\lambda 1,2}$=$\mathbf{A}^{-1}br$ ($\alpha_{\lambda 1}$ = 0.3850 and $\alpha_{\lambda 2}$ = 0.6151). Note that in our formulation, unlike in de Capitani and Brown (1987), the update of the Gibbs-hyperplane defined by $\Delta\Gamma_j$ is achieved using the PGE approach (Eqs. 26, 27 and 28) modified for mixing on crystallographic sites.